SAND2019-6079R

Modeling Validation Exercises Using the Dry Cask Simulator

Spent Fuel and Waste Disposition

Prepared for
US Department of Energy
Spent Fuel and Waste Science and Technology

R.J.M. Pulido, E.R. Lindgren, S.G. Durbin
Sandia National Laboratories, Albuquerque, NM

A. Zigh, J. Solis
Nuclear Regulatory Commission, Washington, DC

S.R. Suffield, D.J. Richmond, J.A. Fort
Pacific Northwest National Laboratory, Richland, WA

L. E. Herranz, F. Feria, J. Penalva
Centro de Investigaciones Energéticas MedioAmbientales y Tecnológicas (CIEMAT), Madrid (Spain)

M. LLoret, M. Galbán
Empresa Nacional del Uranio, S.A., S.M.E. (ENUSA), Madrid (Spain)

J. Benavides, G. Jiménez
Universidad Politécnica de Madrid (UPM), Madrid (Spain)

January 6, 2020

Milestone No. M2SF-19SN010203035
SAND2019-6079 R

Prepared by
Sandia National Laboratories
Albuquerque, New Mexico 87185 and Livermore, California 94550

Sandia National Laboratories is a multimission laboratory managed and operated by National Technology and Engineering Solutions of Sandia, LLC, a wholly owned subsidiary of Honeywell International, Inc., for the U.S. Department of Energy's National Nuclear Security Administration under contract DE-NA0003525.

ABSTRACT

The U.S. Department of Energy (DOE) established a need to understand the thermal-hydraulic properties of dry storage systems for commercial spent nuclear fuel (SNF) in response to a shift towards the storage of high-burnup (HBU) fuel (> 45 gigawatt days per metric ton of uranium, or GWd/MTU). This shift raises concerns regarding cladding integrity, which faces increased risk at the higher temperatures within spent fuel assemblies present within HBU fuel compared to low-burnup fuel (≤ 45 GWd/MTU). The dry cask simulator (DCS) was previously built at Sandia National Laboratories (SNL) in Albuquerque, New Mexico to produce validation-quality data that can be used to test the validity of the modeling used to determine cladding temperatures in modern vertical dry casks. These temperatures are critical to evaluating cladding integrity throughout the storage cycle of commercial spent nuclear fuel.

In this study, a model validation exercise was carried out using the data obtained from dry cask simulator testing in the vertical, aboveground configuration. Five modeling institutions – Nuclear Regulatory Commission (NRC), Pacific Northwest National Laboratory (PNNL), Centro de Investigaciones Energéticas, MedioAmbientales y Tecnológicas (CIEMAT), and Empresa Nacional del Uranio, S.A., S.M.E. (ENUSA) in collaboration with Universidad Politécnica de Madrid (UPM) – were granted access to the input parameters from SAND2017-13058R, "Materials and Dimensional Reference Handbook for the Boiling Water Reactor Dry Cask Simulator", and results from the vertical aboveground BWR dry cask simulator tests reported in NUREG/CR-7250, "Thermal-Hydraulic Experiments Using A Dry Cask Simulator". With this information, each institution was tasked to calculate minimum, average, and maximum fuel axial temperature profiles for the fuel region as well as the axial temperature profiles of the DCS structures. Transverse temperature profiles and air mass flow rates within the dry cask simulator were also calculated. These calculations were done using modeling codes (ANSYS FLUENT, STAR-CCM+, or COBRA-SFS), each with their own unique combination of modeling assumptions and boundary conditions. For this validation study, four test cases of the vertical, aboveground dry cask simulator were considered, defined by two independent variables – either 0.5 kW or 5 kW fuel assembly decay heat, and either 100 kPa or 800 kPa internal helium pressure.

For the results in this report, each model was assigned a model number. Three of the models used porous media model representations of the fuel, two models used explicit fuel representations, and one model used an explicit subchannel representation of the fuel. Even numbers were assigned to explicit fuel models and odd numbers were assigned to porous media models. The plots provided in Chapter 3 of this report show the axial and transverse temperature profiles obtained from the dry cask simulator experiments in the aboveground configuration and the corresponding models used to describe the thermal-hydraulic behavior of this system. The tables provided in Chapter 3 illustrate the closeness of fit of the model data to the experiment data through root mean square (RMS) calculations of the error in peak cladding temperatures (PCTs), average fuel temperatures across six axial levels, transverse temperatures across the PCT locations for the four test cases, and air mass flow rates.

The peak cladding temperature is typically the most important target variable for cask performance, and all models capture the PCT within 5% RMS error. Two models show comparable fits to experimental results when considering the combined RMS error of all target variables. Since one uses a porous media representation of the fuel while the other uses an explicit fuel representation, it can be concluded that the porous media fuel representation can achieve modeling calculation results of peak cladding temperatures, average fuel temperatures, transverse temperatures, and air mass flow rates that are comparable to explicit fuel representation modeling results.

This page is intentionally left blank.

ACKNOWLEDGEMENTS

The authors would like to gratefully acknowledge the hard work and commitment to excellence of Shannon Zubersky, William Chavez, and Greg Koenig, which made the success of this project possible.

This work was conducted under the Department of Energy Spent Fuel and Waste Science and Technology campaign. Sylvia Saltzstein (8845) and Geoff Freeze (8843) are to be commended for exceptional project leadership.

This page is intentionally left blank.

CONTENTS

LIST OF FIGURES

LIST OF TABLES

This page is intentionally left blank.

REVISION HISTORY

Revision	Date	Comments
0	05/30/2019	Original issuance
1	01/06/2020	Updated DCS fuel assembly maximum temperature profile plots in Figure 3.2, Figure 3.4, Figure 3.6, and Figure 3.8

This page is intentionally left blank.

ACRONYMS

BWR	Boiling Water Reactor
CFD	Computational Fluid Dynamics
CIEMAT	Centro de Investigaciones Energéticas, MedioAmbientales y Tecnológicas
CYBL	Cylindrical Boiling
DCS	Dry Cask Simulator
DCSS	Dry Cask Storage System
DOE	U.S. Department of Energy
ENUSA	Empresa Nacional del Uranio, S.A., S.M.E.
GWd	Gigawatt day
HBU	High Burnup
INEL	Idaho National Engineering Laboratory
ISFSI	Independent Spent Fuel Storage Installation
MAWP	Maximum Allowable Working Pressure
MSB	Multi-assembly Sealed Basket
MTU	Metric Ton of Uranium
NE	Nuclear Energy
NRC	Nuclear Regulatory Commission
PCT	Peak Cladding Temperature
PNNL	Pacific Northwest National Laboratory
PWR	Pressurized Water Reactor
R&D	Research & Development
SFWD	Spent Fuel and Waste Disposition
SFWST	Spent Fuel and Waste Science and Technology
SNF	Spent Nuclear Fuel
TAN	Test Area North
TC	Thermocouple
UPM	Universidad Politécnica de Madrid

This page is intentionally left blank.

MODELING VALIDATION EXERCISES USING THE DRY CASK SIMULATOR

This report fulfills milestone M2SF-19SN010203035 in the Spent Fuel and Waste Science and Technology work package (SF-19SN01020303). This work was sponsored under the Department of Energy's (DOE) Office of Nuclear Energy (NE) Spent Fuel and Waste Disposition (SFWD) campaign.

1 INTRODUCTION

Dry cask storage systems (DCSSs) for spent nuclear fuel (SNF) are designed to provide a confinement barrier that prevents the release of radioactive material, maintains SNF in an inert environment, provides radiation shielding, and maintains subcriticality conditions. SNF is initially stored in pools of water for cooling where the water also provides radiation shielding. As these pools approach capacity, dry cask storage systems are becoming the primary alternative for interim storage. After sufficient cooling in pools, SNF is loaded into a canister and placed inside a cask, where the canister is sealed. The dry cask storage system is then decontaminated and dried, and the system is ultimately placed either vertically or horizontally in aboveground or belowground storage. Figure 1.1 shows a diagram for a vertically-oriented, aboveground dry cask storage system.

Source: www.nrc.gov/reading-rm/doc-collections/fact-sheets/storage-spent-fuel-fs.html

Figure 1.1 Typical vertical aboveground dry storage cask system.

The effectiveness of these dry cask storage systems in fulfilling their confinement barrier purpose is evaluated through detailed analytical modeling of their thermal performance. The modeling is carried out by the vendor to demonstrate the performance and regulatory compliance of each DCSS. The Nuclear Regulatory Commission (NRC) then independently verifies these licensing factors. Thermal-hydraulic testing of either full-sized casks or scaled cask analogs is recognized as vital for the validation of design and performance models. Previous studies on single assemblies [Bates, 1986; Irino *et al.*, 1987] and full-scale, multi-assembly casks [Dziadosz *et al*., 1986; McKinnon *et al.*,1986; McKinnon *et al*., 1987; Creer *et al*., 1987; McKinnon *et al*.,1989; McKinnon *et al*., 1992] have contributed to the knowledge base of heat transfer and flow in dry storage casks, which helps with the evaluation of cladding integrity and the definition of regulatory limits for key parameters in these systems, such as peak cladding temperatures (PCTs).

The boiling water reactor (BWR) dry cask simulator (DCS) was built and tested [Durbin and Lindgren, 2018] in a simulated aboveground configuration with a helium backfill to add to the dry storage cask thermal-hydraulic response knowledge base. This was done by obtaining characteristic data under various heat loads, internal canister pressures, and external configurations. The motivation was to determine the influences of elevated helium pressures that have become more prevalent in modern cask designs and the

external convection of aboveground dry cask storage systems not accounted for in previous studies. This test simulated a single, full-length prototypic BWR fuel assembly – a large temperature data set was collected from the 97 thermocouples (TCs) arranged at 0.152 m (6 in.), 0.305 m (12 in.), and 0.610 m (24 in.) intervals. Since tests were completed for the BWR dry cask simulator in 2016, the next step in adding to this knowledge base was to validate models currently used to determine cladding temperatures in vertical dry casks by comparing modeling results to the experimental data.

1.1 Objective

The purpose of this study was to compare models used to determine cladding temperatures in full-scale vertical BWR dry casks. Five modeling institutions – Nuclear Regulatory Commission (NRC), Pacific Northwest National Laboratory (PNNL), Centro de Investigaciones Energéticas, MedioAmbientales y Tecnológicas (CIEMAT), and Empresa Nacional del Uranio, S.A., S.M.E. (ENUSA) in collaboration with Universidad Politécnica de Madrid (UPM) – were granted access to the input parameters from SAND2017-13058R, "Materials and Dimensional Reference Handbook for the Boiling Water Reactor Dry Cask Simulator" [Lindgren and Durbin, 2017], and results from the vertical aboveground BWR dry cask simulator tests reported in NUREG/CR-7250 [Durbin and Lindgren, 2018]. With this information, each institution was tasked to calculate both axial and transverse temperature profiles as well as air mass flow rates within the dry cask simulator using modeling codes, each with their own unique combination of modeling assumptions and boundary conditions.

1.2 Previous Studies

NUREG-2152 [Zigh and Solis, 2013] states that model validation exercises examine whether the physical models used in computational fluid dynamics (CFD) calculations correlate with real-world observations, and that a basic validation strategy involves identifying and quantifying any errors and uncertainties that arise through the comparison of modeling results to experimental data. These types of validation exercises can be used for any type of modeling code. Numerous studies have contributed to the correlations between computer modeling simulation outputs and experimental data from dry cask investigations, with some initial studies done on single assemblies and later studies done on full-scale, multi-assembly systems.

1.2.1 Small Scale, Single Assembly Model Validation

The COBRA-SFS computer code is "a steady-state, lumped-parameter, finite-difference code which predicts flow and temperature distributions in spent fuel storage systems…by providing solutions to the equations governing mass, momentum, and energy conservation for single-phase incompressible flows" [Lombardo *et al.*, 1986]. It was used to make predictions on the temperature profiles of both an actual spent fuel single assembly and an electrically heated assembly. This study marked the first instance of the COBRA-SFS code being used to study spent fuel. The spent fuel assembly was a discharged 15×15 pressurized water reactor (PWR) assembly from the Florida Power and Light Turkey Point Unit Number 3 reactor with a burnup of 28 GWd/MTU. The decay heat levels were 1.17 kW for air and vacuum fill media and 1.16 kW for helium fill media. The electrically-heated assembly was built to simulate a 15×15 light water reactor PWR fuel assembly, and 18 tests were performed which modified the fill media (air at atmospheric pressure, helium at 6.9 ± 3.5 kPa, vacuum at -610 mm mercury), the test assembly power level (0.5 kW, 1 kW), and the test cask orientation (vertical, horizontal, inclined or 25° from horizontal). Each assembly was instrumented with thermocouples to obtain experimental temperature data during each test run – 20 thermocouples were placed at 5 axial locations on the outer wall, while 15 instrument tubes (each with 7 thermocouples at different axial locations) were placed in the emptied control rod guide tubes to collect axial temperature information within the assembly. To simulate a multi-assembly cask, the outer surfaces of both of the test casks containing the single assemblies were heated to maintain a fixed, elevated wall temperature that simulates the presence of adjacent fuel assemblies. For both cases, the canister was surrounded by a carbon steel liner and was heated to a temperature that would be

expected in a multi-assembly system. Once this elevated temperature reached steady state, temperature data within the assembly was collected.

Blind, or "pre-look", runs of the COBRA-SFS code were first conducted before the tests to judge how accurately the code could predict internal cask temperatures. The predicted peak cladding temperatures for the spent fuel and electrically heated PWR fuel assemblies were within ±10°C and ±27°C, respectively. The discrepancy between the predicted temperatures and the experimental data was primarily attributed to inadequate modeling of the convection in the test casks and an over-prediction of the temperature drop from the fuel tubes to the cask wall. Following the collection of experimental data, post-test optimization simulations were run. For the electrically-heated cask model, when the emissivity was changed from 0.2 to 0.25, better agreement in the fuel tube-to-cask wall temperature difference for both the 0.5 kW and 1 kW cases was found. Although there were still slight discrepancies between the COBRA-SFS predictions and the experimental data (due to the increased friction factor applied to the downcomer assembly, which aided in computational stability), the post-test predicted peak rod temperatures lay within ± 3°C and ± 15°C for the spent fuel and electrically-heated assemblies, respectively. Therefore, the optimized code was shown to have improved capability of predicting temperatures in the two test assemblies.

1.2.2 Full Scale, Multi Assembly Model Validation

The transient analysis capability of COBRA-SFS underwent a verification and validation study through a comparison of model results to experimental data from the multi-assembly TN24P and PSN/VSC-17 casks that were tested at the Idaho National Engineering Laboratory (INEL) Test Area North (TAN) facility [Rector *et al*., 1998]. For the TN24P test, the transient condition involved changing the backfill gas from helium to air, while for the PSN/VSC-17 test, the transient condition involved opening all backfill gas vents on the air annulus between the multi-assembly sealed basket (MSB) and the outer shell. The temperatures calculated by COBRA-SFS were found to be well within experimental uncertainty throughout the entire transient period for the TN24P test. For the PSN/VSC-17 test, the calculated temperatures were within experimental uncertainty for approximately 70 hours elapsed time in the transient state, after which the model-calculated temperatures began to trend more conservatively than the measured temperatures.

The thermal performance of the HI-STORM 100 dry storage cask was studied using ANSYS/FLUENT [Li and Liu, 2016]. The HI-STORM cask contained 32 PWR spent fuel assemblies with a total decay heat load of 34 kW in a weld-sealed canister. This work numerically explored the effects of the canister fill gas (nitrogen or helium), the internal pressure (1-6 atm), and the basket material (stainless steel or aluminum alloy) on the modeled temperature profiles and peak cladding temperatures present in the cask. The results of each variable change were presented using temperature contours generated by ANSYS/FLUENT. Simulation results were validated by comparing data of the canister surface temperatures between the simulations and the data measured at Diablo Canyon [Waldrop and Kessler, 2014] and simulation results from Cuta and Adkins [2014]. The study found that the use of nitrogen, which has a much lower thermal conductivity than helium but a higher density, enhanced natural convection. The internal pressure increase from 1 to 6 atm changed the axial temperature distribution and the resulting location of the PCT from a system with conduction as the dominant heat transfer mechanism (where the PCT would be located in the middle of the axial length) to one with convection as the dominant mechanism (where the PCT would be located towards the top of the axial length due to the rising of the heated fill gas). Using an aluminum alloy as the basket material, which has a much higher thermal conductivity than stainless steel, in conjunction with using nitrogen instead of helium, resulted in much faster heat transfer away from the cask and thus lower PCTs.

One of the most recent investigations into the capability of CFD models to predict dry cask experimental data involves the modeling of transverse and axial temperature profiles of a dry storage cask loaded with high-burnup fuel. The Spent Fuel and Waste Science and Technology (SFWST) research and

development (R&D) program of the U.S. Department of Energy (DOE) is conducting a high-burnup fuel demonstration using an Orano TN-32B dry storage cask at the North Anna Nuclear Power Station's Independent Spent Fuel Storage Installation (ISFSI), with the goal being to load the cask with high-burnup fuel (up to 55.5 GWd/MTU) that would produce temperatures as close as possible to the 400°C NRC regulatory limit specified in Interim Staff Guidance 11, Revision 3 [NRC, 2003]. PNNL [Fort *et al.*, 2018] conducted a thermal modeling study in order to assist with proposed cask loading patterns and to obtain "best estimate" temperatures that would be present during the initial loading of the cask and the subsequent 10-year storage period. They conducted modeling studies with the purpose of obtaining predictions of cladding temperatures during the assembly load planning, pre-loading, post-loading, and initial/final storage period stages. The COBRA-SFS subchannel code and the STAR-CCM+ CFD code were used to model the TN-32B cask. The COBRA-SFS code modeled the fuel and basket region in detail (and the external regions in a simplified manner), while the STAR-CCM+ code modeled the basket and surrounding components in detail (and the fuel region as a porous media). The cask was instrumented with thermocouple lances, and the results from the two models were compared to measured temperatures. It was found that for the best-estimate post-drying case, both the COBRA-SFS and STAR-CCM+ codes overpredicted the peak cladding temperatures in the TN-32B cask, with axial temperature profiles from blind model predictions indicating a positive difference between the predicted and measured temperatures for nearly all axial levels in the assemblies whose temperatures were measured. Using best estimates for the ambient temperature and the decay heat, the highest peak cladding temperature from the modeling that was predicted for the initial storage conditions was 259°C while the experimental PCT from thermocouple measurements was 229°C.

1.3 Uniqueness of Current Study

This study contains unique features that differ from previous studies on modeling predictions of dry cask experimental data. First and foremost, the dry cask simulator in this study is set up to incorporate the integral effects of external ventilation and internal natural convection within the system. The mock assembly itself is geometrically prototypic and accommodates a helium backfill gas with elevated pressures up to 800 kPa.

For the modeling, five institutions (NRC, PNNL, CIEMAT, and ENUSA-UPM) were enlisted to provide their own unique approaches to capturing the temperature profiles and air mass flow rates within the BWR dry cask simulator in the aboveground configuration. For these comparisons, four test cases of the vertical, aboveground dry cask simulator were considered, defined by two independent variables – either 0.5 kW or 5 kW fuel assembly decay heat, and either 100 kPa or 800 kPa internal helium pressure. The test matrix for experiment and model data comparison is shown in Table 1.1. Low and high decay heats and pressures were chosen to cover the range of temperatures and natural convection conditions that would be observed in a dry storage cask. For all cases, the modelers obtained peak cladding temperatures, average fuel axial temperature profiles across six axial levels, transverse temperatures across the PCT locations for the four test cases, and air mass flow rates external to the canister. The modeling codes used by each institution encompassed a variety of computational approaches to determining these target variables, which were characterized by the software used (ANSYS FLUENT, STAR-CCM+, or COBRA-SFS) and the use of either porous media or explicit fuel models to describe the DCS fuel assembly.

Table 1.1 DCS experiment test matrix for model validation.

Power (kW)	Pressure (kPa)
0.5	100
0.5	800
5.0	100
5.0	800

2 APPARATUS AND PROCEDURES

This chapter provides a summary of the experimental dry cask simulator that generated the data for model comparison. The various subsystems, components and methods used to construct the experimental apparatus are described in detail elsewhere [Durbin, *et al.*, 2016]. The test apparatus design was guided by an attempt to match critical dimensionless groups with prototypic systems as reasonably as possible, with a focus on Reynolds, Rayleigh, and Nusselt numbers. The dimensional analyses revealed that a scaling distortion in simulated assembly power would be necessary to span the thermal-hydraulic response of a full-sized spent fuel storage cask. This need for additional decay heat is reasonable given the higher external surface-area-to-volume ratio of a single assembly arrangement as in the DCS compared to a modern canister with up to 89 assemblies. A more rigorous treatment of this scaling distortion is available for further details [Durbin, *et al.*, 2016].

Each phase of experimental apparatus design and implementation was also guided by extensive, meticulous CFD modeling that is not explicitly detailed in this report. A brief description and example of modeling results may be found in Zigh, *et al.* [2017]. As an example, these models provided information on the flow profile development and thermal gradients that were critical to the optimization of flow straightening and hot wire anemometer placements.

2.1 General Construction

The general design details are shown in Figure 2.1. An existing electrically heated but otherwise prototypic BWR Incoloy-clad test assembly was deployed inside of a representative storage basket and cylindrical pressure vessel that represents the canister. The symmetric single assembly geometry with well-controlled boundary conditions simplified interpretation of results. A custom configuration of outer concentric ducting was used to mimic conditions for an aboveground storage configuration of vertical, dry cask systems with canisters. Radial and axial temperature profiles were measured for a wide range of decay power and canister pressures. Of particular interest was the evaluation of the effect of increased helium pressure on thermal response for the aboveground configuration. External air mass flow rates were calculated from measurements of the induced air velocities in the external ducting.

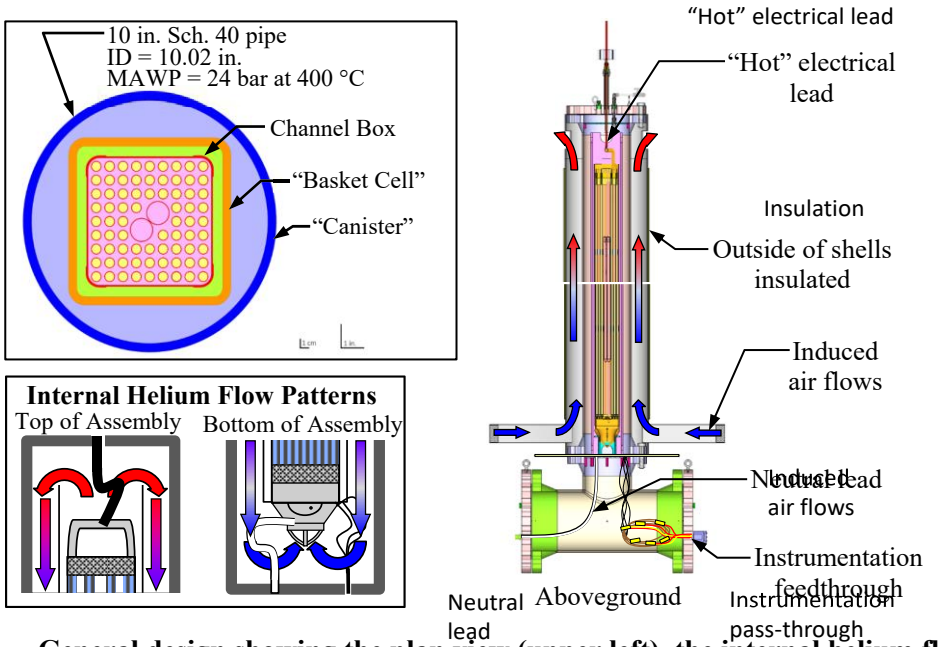

Figure 2.1 General design showing the plan view (upper left), the internal helium flow (lower left), and the external air flow for the aboveground configuration (right).

The test configurations were assembled and operated inside of the Cylindrical Boiling (CYBL) test facility, which is the same facility used for earlier fuel assembly studies [Lindgren and Durbin, 2007]. CYBL is a large, stainless steel containment vessel repurposed from earlier flooded containment/core retention studies sponsored by DOE. Since then, CYBL has served as an excellent general-use engineered barrier for the isolation of high-energy tests. The outer vessel is 5.1 m in diameter and 8.4 m tall (16.7 ft. in diameter and 27.6 ft. tall) and constructed with 9.5 mm (0.375 in.) thick, stainless steel walls. Figure 2.2 shows a scaled diagram of the CYBL facility with the aboveground version of the test DCS inside.

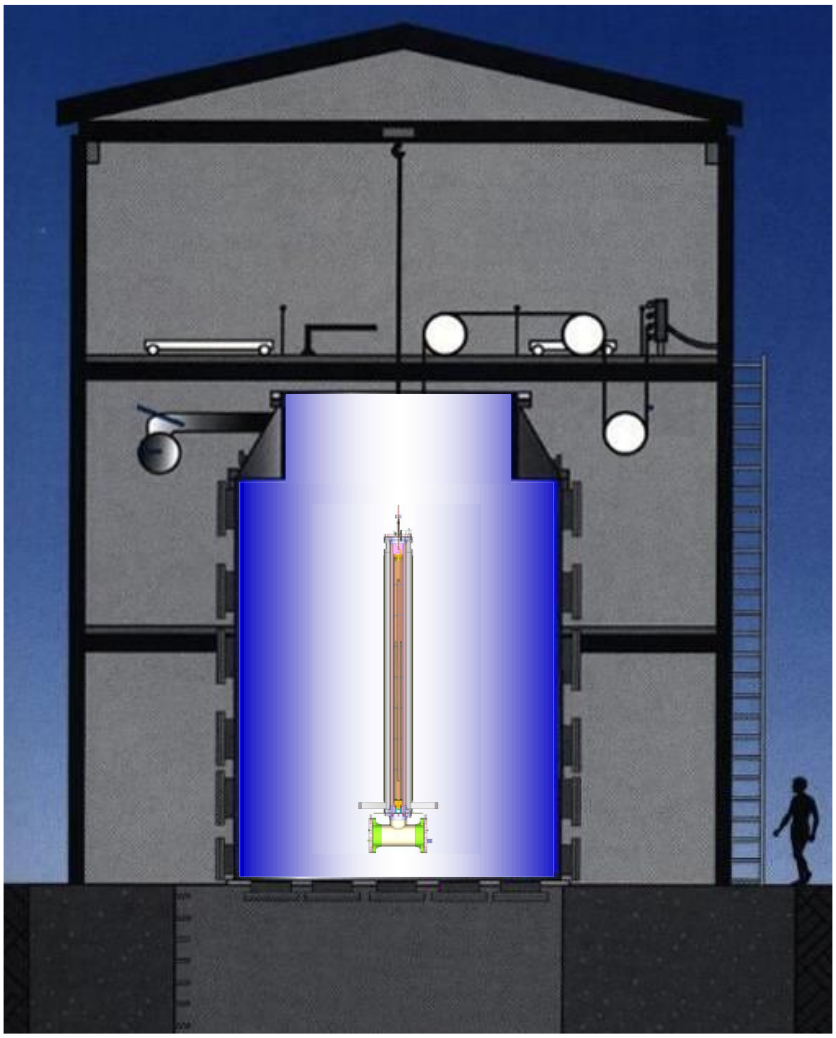

Figure 2.2 CYBL facility housing the aboveground version of the BWR dry cask simulator.

2.2 Design of the Heated Fuel Bundle

The highly prototypic fuel assembly was modeled after a 9×9 BWR. Commercial components were purchased to create the assembly including the top and bottom tie plates, spacers, water rods, channel box, and all related assembly hardware (see Figure 2.3). Incoloy heater rods were substituted for the fuel rod pins for heated testing. Due to fabrication constraints the diameter of the Incoloy heaters was slightly smaller than prototypic pins, 10.9 mm versus 11.2 mm. The dimensions of the assembly components are listed below in Table 2.1.

Table 2.1 Dimensions of assembly components in the 9×9 BWR.

Description	Lower (Full) Section	Upper (Partial) Section
Number of rods	74	66
Full rod length including pins (m)	3.96	
Partial rod length including pins (m)	2.61	
Pin diameter (mm)	10.9	
Pin pitch (mm)	14.4	
Pin separation (mm)	3.48	
Water rod OD (main section) (mm)	24.9	
Water rod ID (mm)	23.4	
Nominal channel box ID (mm)	134	
Nominal channel box OD (mm)	139	

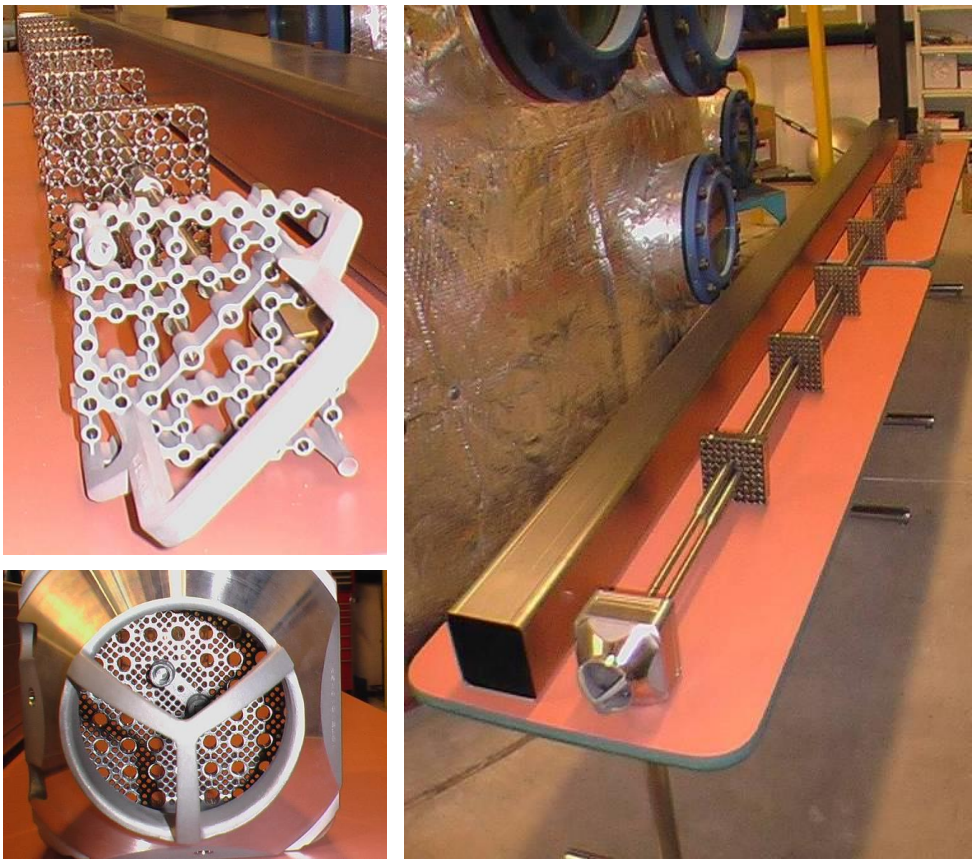

Figure 2.3 Typical 9×9 BWR components used to construct the test assembly including top tie plate (upper left), bottom tie plate (bottom left) and channel box and spacers assembled onto the water rods (right).

2.3 Instrumentation

The test apparatus was instrumented with thermocouples (TCs) for temperature measurements, pressure transducers to monitor the internal vessel pressure, and hot wire anemometers for flow velocity measurement in the exterior ducting. Volumetric flow controllers were used to calibrate the hot wire

probes. Voltage, amperage, and electrical power transducers were used for monitoring the electrical energy input to the test assembly.

Ninety-seven thermocouples were previously installed on the BWR test assembly. Details of the BWR test assembly and TC locations are described elsewhere [Lindgren and Durbin, 2007]. Additional thermocouples were installed on the other major components of the test apparatus such as the channel box, storage basket, canister wall, and exterior air ducting. TC placement on these components is designed to correspond with the existing TC placement in the BWR assembly. Ambient temperatures were also measured – these temperatures varied by 6 K at most during steady-state conditions for the four test cases [Durbin and Lindgren, 2018].

The thermocouples used were ungrounded junction Type K with an Incoloy sheath diameter of 0.762 mm (0.030 in.) held in intimate contact with the cladding by a thin Nichrome shim. This shim is spot welded to the cladding as shown in Figure 2.4. The TC attachment method allows the direct measurement of the cladding temperature.

Figure 2.4 Typical TC attachment to heater rod.

Hot wire anemometers were chosen to measure the inlet flow rate because this type of instrument is sensitive and robust while introducing almost no unrecoverable flow losses. Due to the nature of the hot wire measurements, best results are achieved when the probe is placed in an isothermal, unheated gas flow.

2.3.1 Thermocouple (TC) Locations

The existing electrically heated prototypic BWR Incoloy-clad test assembly was previously instrumented with thermocouples in a layout shown in Figure 2.5. The assembly TCs are arranged in axial and radial arrays. The axial cross-section is depicted in Figure 2.5a and radial cross-sections are shown in Figure 2.5b. The axial array A1 has TCs nominally spaced every 0.152 m (6 in.) starting from the top of the bottom tie plate (z_o = 0 reference plane). Axial array A2 has TCs nominally spaced every 0.305 m (12 in.) and the radial arrays are nominally spaced every 0.610 m (24 in.). The spacings are referred to as nominal due to a deviation at the 3.023 m (119 in.) elevation because of interference by a spacer. Note that the TCs in the axial array intersect with the radial arrays.

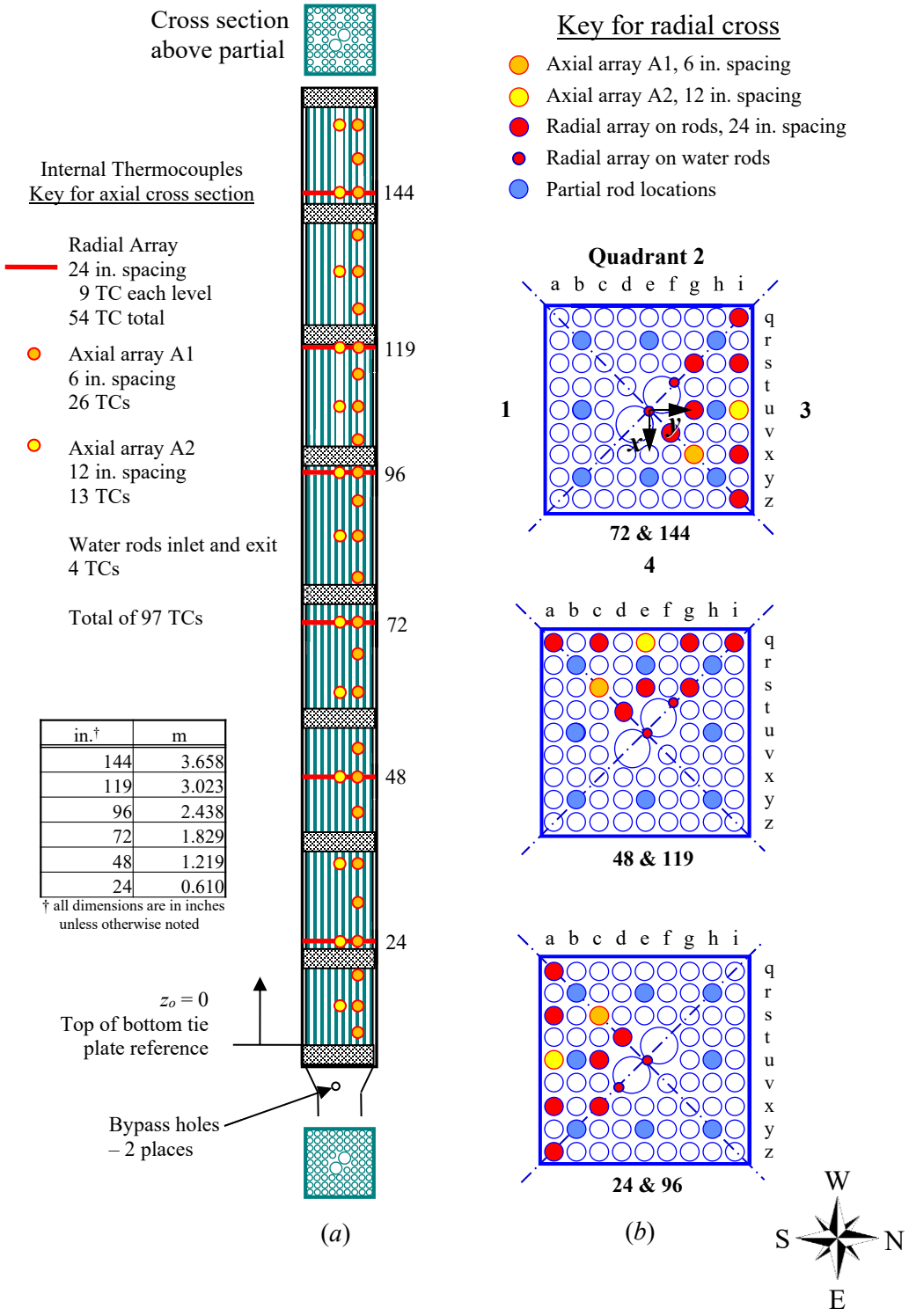

Figure 2.5 Experimental BWR assembly showing as-built *a*) axial and *b*) lateral thermocouple locations.

Based on the need to optimally balance the TC routing through the assembly, the axial and radial array TCs were distributed among three separate quadrants relying on the assumption of axial symmetry. No TCs were installed in quadrant 4 (see Figure 2.5b). TCs on the concentric components surrounding the

assembly (channel box, storage basket, canister (or vessel), outer shell) were placed at the same elevations and on the corresponding quadrant faces as the TCs in the assembly bundle. Additionally, these outer components also had TCs installed at 0.610 m (24 in.) intervals along the quadrant 4 face.

Figure 2.6 shows the definition of the reference coordinate system. The reference origin is defined as being in the center of the top of the bottom tie plate. The *x*-axis is positive in the direction of Quadrant 4 and negative in the direction of Quadrant 2. The *y*-axis is positive in the direction of Quadrant 3 and negative in the direction of Quadrant 1.

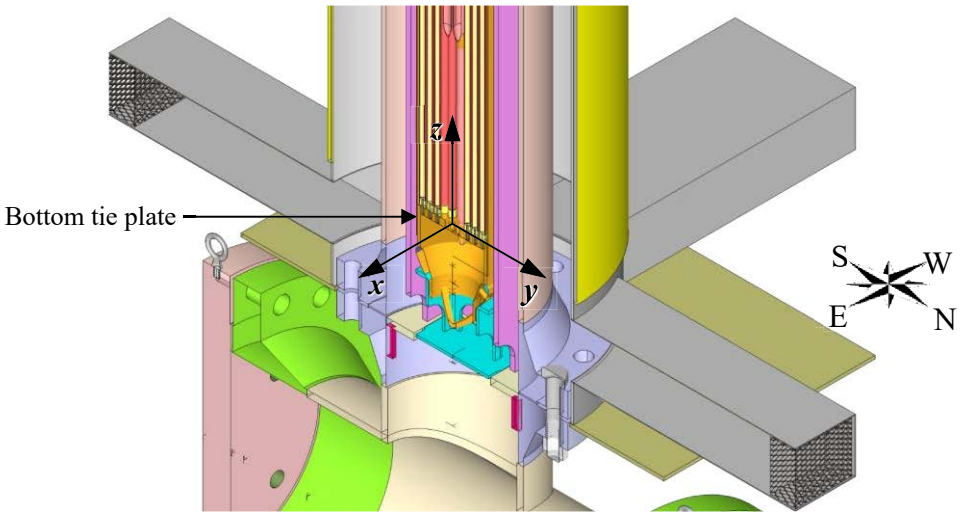

Figure 2.6 Definition of coordinate references in test apparatus.

2.3.2 Pressure Measurement and Control

Two high-accuracy 0 to 3447 kPa (0 to 500 psia) absolute pressure transducers (OMEGA PX409-500A5V-XL) were installed in the lower reducing tee. At least one of these transducers was operational for each heated test. A constant helium pressure control system was implemented using the high accuracy absolute pressure transducers, three low flow needle valves, and three positive shutoff actuator valves under control of the LabView DAC system. Two actuator valves (vent) controlled helium flow out of the vessel, and the third valve (fill) controlled helium flow into the vessel. As the vessel heated up, the expanding helium was vented out the first actuator and needle valve to maintain a constant pressure. A second vent valve (overflow) activated if the vessel continued to pressurize. As steady state was reached, the small helium leak slowly reduced the helium pressure at which point the control system opened the third actuator valve (fill) to allow a small helium flow through the third needle valve. Overall, the pressure control system maintained the helium pressure constant to ±0.3 kPa (0.044 psi).

2.3.3 Air Mass Flow Rate

2.3.3.1 Hot Wire Anemometers

The method for determining the induced air flow in the aboveground configuration used hot wire anemometers to measure inlet air velocity and subsequently calculate an overall air mass flow rate.

The type of hot wire anemometer used for this testing was TSI model 8455. The sensor tip details are shown in Figure 2.7. For scale, the largest shaft diameter shown was 6.4 mm (0.25 in.). The sensing element of the model 8455 is protected inside of an open cage and is sensitive to flows down to 0.13 m/s (25 ft/min) with a fast response time of 0.2 seconds.

Hot wire anemometers were chosen to measure the inlet flow rate because this type of instrument is sensitive and robust while introducing almost no unrecoverable pressure loss. Due to the nature of the hot

wire measurement, for best results the probes were placed in the gas flow at the flow inlets where temperature and thermal gradients were minimal.

Figure 2.7 Photograph of the hot wire anemometer tip.

Details on the processing of hot wire anemometer outputs into calculated air mass flow rates are included in the DCS thermal-hydraulic results report [Durbin and Lindgren, 2018].

2.3.3.2 Flow Straightening

To obtain the most stable and repeatable measurements possible, a honeycomb element was inserted into the inlets of the assembly. This honeycomb served to align the flow in the desired direction and reduce any flow disturbances on the hot wire measurements. As shown in Figure 2.8, a plastic honeycomb element was chosen with a cell diameter, wall thickness, and flow length of 3.8, 0.1, and 51.6 mm (0.150, 0.004, and 2.030 in.), respectively. This type of flow straightening element was found to provide the greatest reduction in hot wire fluctuations while introducing the smallest pressure drop to the system. The effective friction coefficient for this honeycomb material is described in NUREG-2208 [Zigh and Solis, 2017] and is based on Darcy's Law (Equation 2-1):

$$\Delta P = D \cdot \mu \cdot L \cdot V \tag{2-1}$$

Here, ΔP is the pressure drop in a porous media over the length L, D is the friction coefficient, μ is the dynamic viscosity, L is the flow length, and V is the average velocity within the porous media. The friction coefficient was found to be 2.7E6 m^{-2} for porous media in CFD simulations.

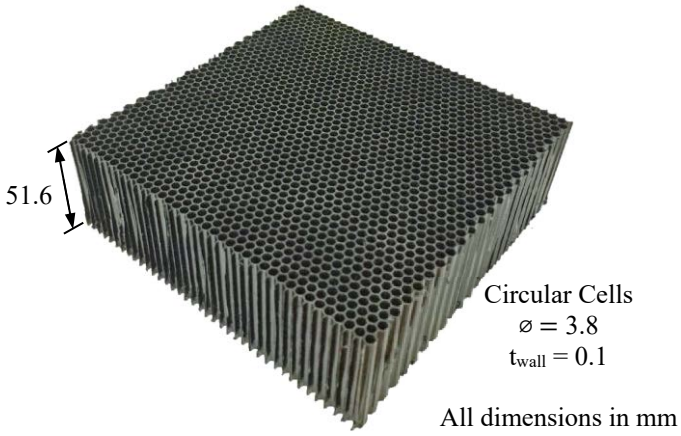

Figure 2.8 Photograph of the honeycomb element used for flow straightening.

2.3.3.3 Aboveground Air Flow Measurement

The inlet and hot wire arrangement for the aboveground configuration is shown in Figure 2.9. Four rectangular ducts with as-built cross-sectional dimensions of 0.229 m (9.03 in.) by 0.100 m (3.94 in.) conveyed the inlet flow into the simulated cask. Three TSI Model 8455 hot wire anemometers were used for these tests. Hot wire anemometers were located 0.229 m (9.00 in.) downstream from the inlet of each duct along the centerline of flow.

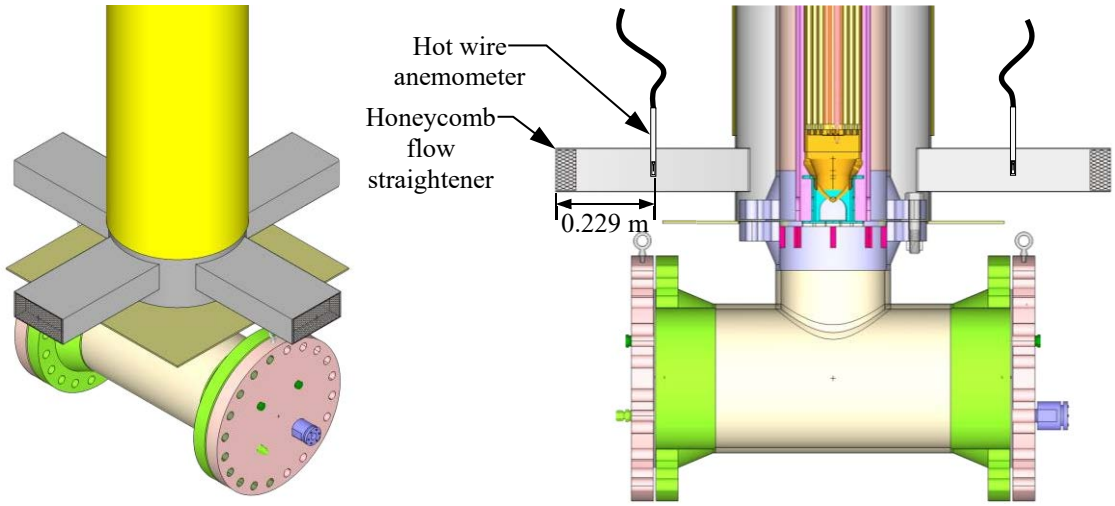

Figure 2.9 Aboveground configuration showing the location of the hot wire anemometer.

3 RESULTS

3.1 Model Summary

A brief summary of the models used for the validation exercises is shown in Table 3.1. This table outlines the code used for each model. It also shows how each code represents the DCS fuel assembly, using either an explicit model that represents the fuel rods and spacers in detail, a porous media model where the fuel is homogenized into a simplified volume with corresponding inertial and frictional loss coefficients, or an explicit subchannel model where the fuel is divided into a number of flow paths or channels. The modeling codes can be grouped into one of three categories – CFD detailed modeling, CFD porous media modeling, and subchannel modeling – which are defined by their approaches. Figure 3.1 illustrates these three categories.

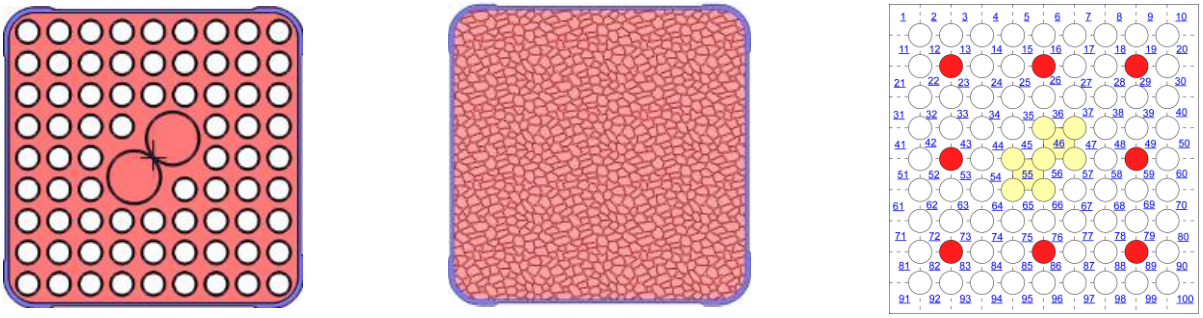

(a) (b) (c)

Figure 3.1 Visual representations of (a) CFD explicit modeling, (b) CFD porous media modeling, and (c) explicit subchannel modeling of the DCS fuel assembly.

Table 3.1 also details the flow treatments the codes utilize in both the fuel assembly and DCS outer structure regions – both the internal helium flow and the external air flow were modeled as either laminar or turbulent. Radiation and convection are treated independently for the explicit models, but for the porous media models, radiation and convection are both accounted for by using an effective thermal conductivity (k_{eff}). The input parameters for the materials and flow gases in each code were taken from the DCS handbook [Lindgren and Durbin, 2017]. The treatment of the helium depends on the code and is either temperature-dependent only or temperature- and pressure-dependent in the ideal gas assumption. The table briefly outlines the initial and boundary conditions for the experiment simulations, such as how the flow straightening element is treated. The table also describes the type of symmetry used in each model for computational efficiency purposes. More details on each code can be found in the Appendices.

Table 3.1 Summary of modeling parameters.

Modeling Contributor	Code Type	Fuel Representation	Internal Flow Treatments	Cooling Air Flow Treatment	Input Parameters	Initial/Boundary Conditions	Cross-Sectional Symmetry
NRC	CFD	Porous media	Laminar helium flow; k_{eff} includes conduction and radiation only	Turbulent air flow – standard k-ε low-Reynolds	Materials properties taken from DCS handbook (helium and air treated as ideal gas)	Flow straightener modeled as porous media; porous loss coefficients calculated from isothermal pressure drop method	1/4
PNNL	CFD	Explicit	Laminar helium flow, internal radiation applied	Turbulent air flow – standard k-ε low-Reynolds	Materials properties taken from DCS handbook (air treated as ideal gas and helium properties are T-dependent only)	Uniform heat load across full and partial length heater rods; natural convection coefficient correlations used for external region	1/4
PNNL	CFD	Porous media	Laminar helium flow; k_{eff} includes conduction and radiation only	Turbulent air flow – standard k-ε low-Reynolds	Materials properties taken from DCS handbook (air treated as ideal gas and helium properties are T-dependent only)	Porous loss coefficients calculated from flow straightener and fuel assembly submodels	1/4
PNNL	Subchannel	Quasi-3D rods	Laminar helium flow	Closure model not applicable	Materials properties taken from DCS handbook (helium and air properties are T-dependent only)	Flow straightener treated with a loss coefficient; standard cylindrical convection correlation; no external heating due to radiation	Full
CIEMAT	CFD	Porous media	Laminar helium flow; k_{eff} includes conduction and radiation only	Turbulent air flow – k-ω SST	Helium thermo-physical properties are all T-dependent except helium density (helium treated as ideal gas); emissivity from DCS handbook	Churchill and Chu correlations of natural convective heat transfer used for outer surfaces; bottom blind flange considered adiabatic	1/8
ENUSA-UPM	CFD	Explicit	Turbulent helium flow – realizable k-ε (shear-driven), power deposited on inner cladding faces	Turbulent air flow – realizable k-ε (shear-driven)	Materials properties taken from DCS handbook (helium and air treated as ideal gas); helium and air properties are T-dependent	Flow straightener modeled as pressure jump between air inlet/outlet	1/2

3.2 Experiment Versus Model Data Comparison

The results of the dry cask simulator thermal-hydraulic experiments can be found in NUREG/CR-7250, "Thermal-Hydraulic Experiments Using A Dry Cask Simulator" [Durbin and Lindgren, 2018]. The experiments involved the use of thermocouples to measure temperature profiles during experimental runs for four different cases of heater rod powers (representative of spent fuel decay powers) and helium pressures (representing both ambient and elevated pressures) – the four cases are shown in Table 1.1. The thermocouples were placed axially at 0.152 m (6 in.) intervals and radially at select axial levels spaced nominally 0.610 m (24 in.) apart, with the thermocouple locations specified in Section 2.3.1. Hot wire anemometers were used to measure air flow velocities in three of the inlet ducts – air mass flow rates were derived from the voltage readings of these devices, which corresponded to mass flow rates.

For the results in this report, each model was assigned a model number. Three of the models used porous media model representations of the fuel, two used explicit fuel representations, and one used an explicit subchannel representation of the fuel. Even numbers were assigned to explicit models and odd numbers were assigned to porous media models. These model numbers are reflected in the plots and tables in this report. The model numbers do not correspond to the ordering of the models in Table 3.1.

The steady state axial temperature profile measured in the fuel during the 0.5 kW, 100 kPa test case is presented as axial level versus temperature in Figure 3.2 along with the corresponding results from the six modeling efforts. The error bars on the experimental data represents an estimated uncertainty of 1% of the overall PCT for the temperature measurement. The figure of the experimental apparatus on the far right is scaled to match the axial levels on the y-axes of the plots. The reference plane for axial height is defined at the top of the bottom tie plate. The data is taken from the six radial arrays spaced nominally 0.610 m (24 in.) apart shown in Figure 2.5. Three plots are presented for the minimum, weighted average, and maximum temperature measured on each radial array. An inset of the assembly cross-section indicates the nominal location of the temperatures shown by a blue star or triangle. The left plot shows the minimum temperature measured or modeled on each radial array. The center plot shows the mass-weighted average of all temperatures measured or modeled on each radial array. The right plot shows the maximum temperature measured or modeled on each radial array. The PCT located at any axial position is denoted by a larger solid symbol for both the data and the model predictions. Figure 3.4, Figure 3.6, and Figure 3.8 present the same information but for the remaining test cases of 0.5 kW and 800 kPa, 5 kW and 100 kPa, and 5 kW and 800 kPa, respectively. Note that the temperature scales are different for each set of plots.

The steady state axial temperature profiles measured in each of the outer four components during the 0.5 kW, 100 kPa test case are presented as axial level versus temperature in Figure 3.3 along with the corresponding results from the six modeling efforts. A quarter cross-section of the dry cask simulator fuel assembly and its outlying structures are inset on the bottom corners of each plot. The blue stars in these insets indicate the component that each plot corresponds to, whether it is the channel box, basket, pressure vessel, or shell (overpack). Again, the figure of the experimental apparatus on the far right is scaled to match the axial levels shown in the plots. Figure 3.5, Figure 3.7, and Figure 3.9 present the same information but for the remaining test cases of 0.5 kW and 800 kPa, 5 kW and 100 kPa, and 5 kW and 800 kPa, respectively.

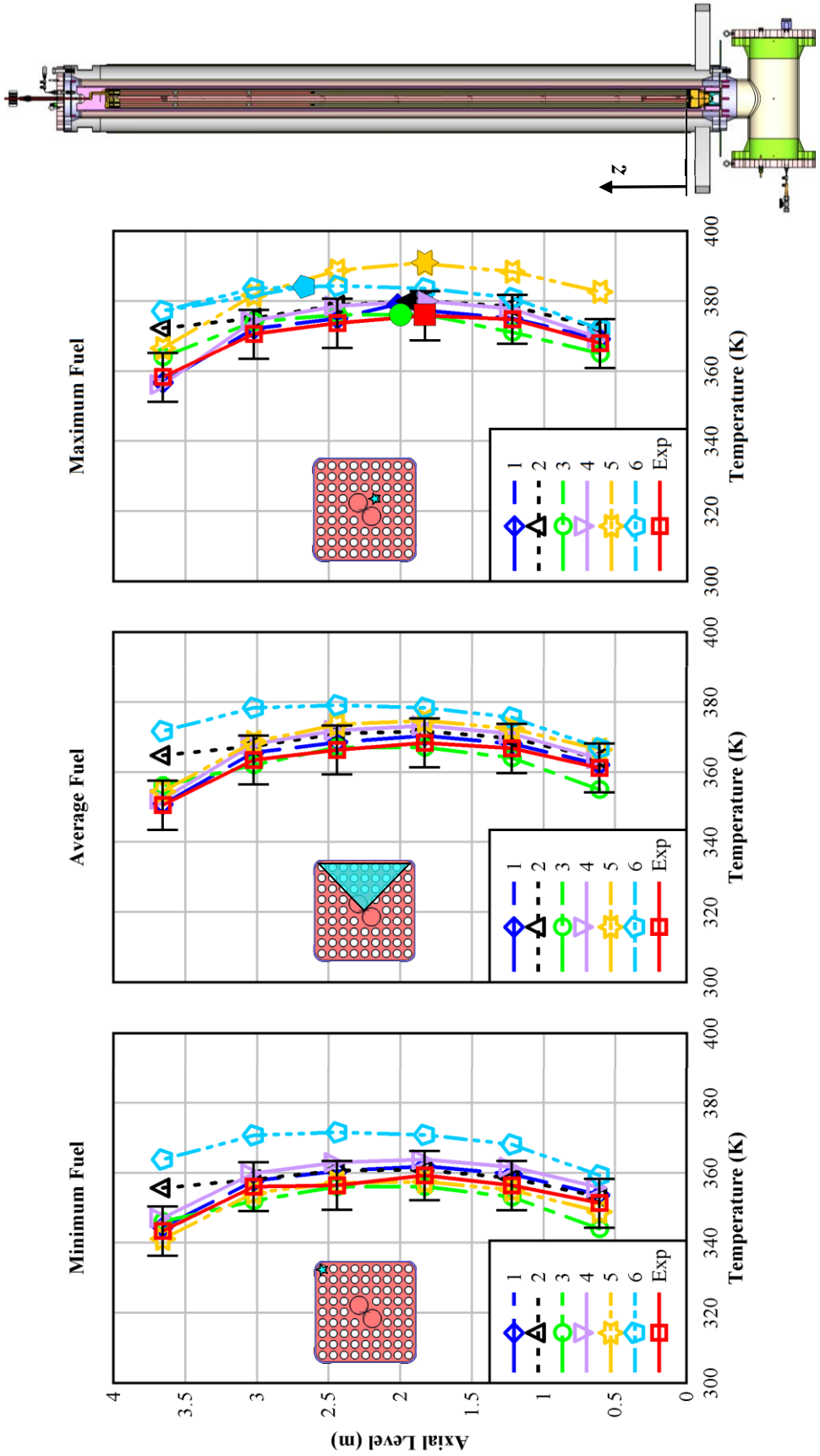

Figure 3.2 DCS fuel assembly axial temperature profile comparisons between experiment and model results for the 0.5 kW, 100 kPa test case. Peak cladding temperatures and their axial locations are represented by the large symbols in the maximum fuel temperature profile.

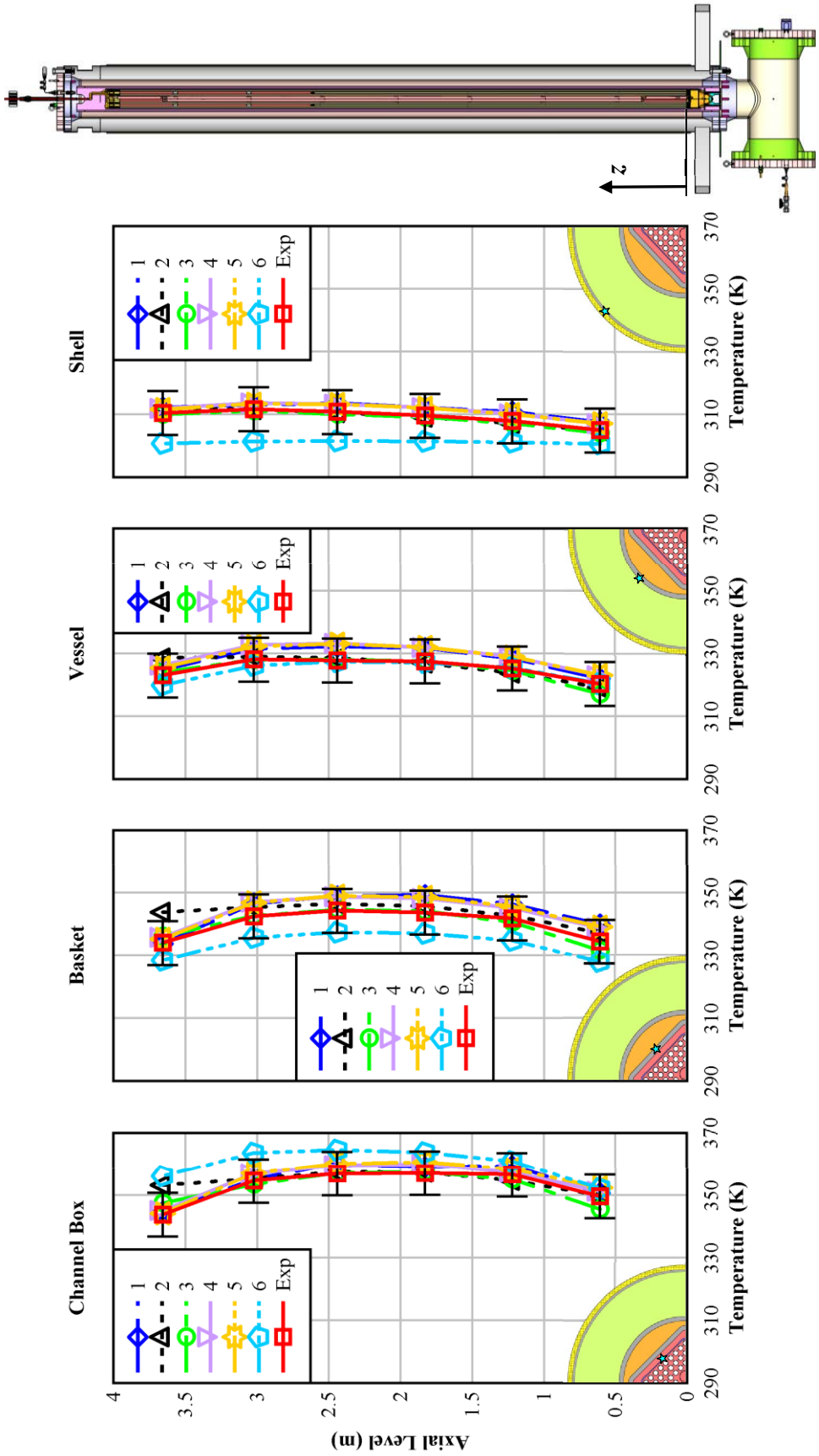

Figure 3.3 DCS structure axial temperature profile comparisons between experiment and model results for the 0.5 kW, 100 kPa test case.

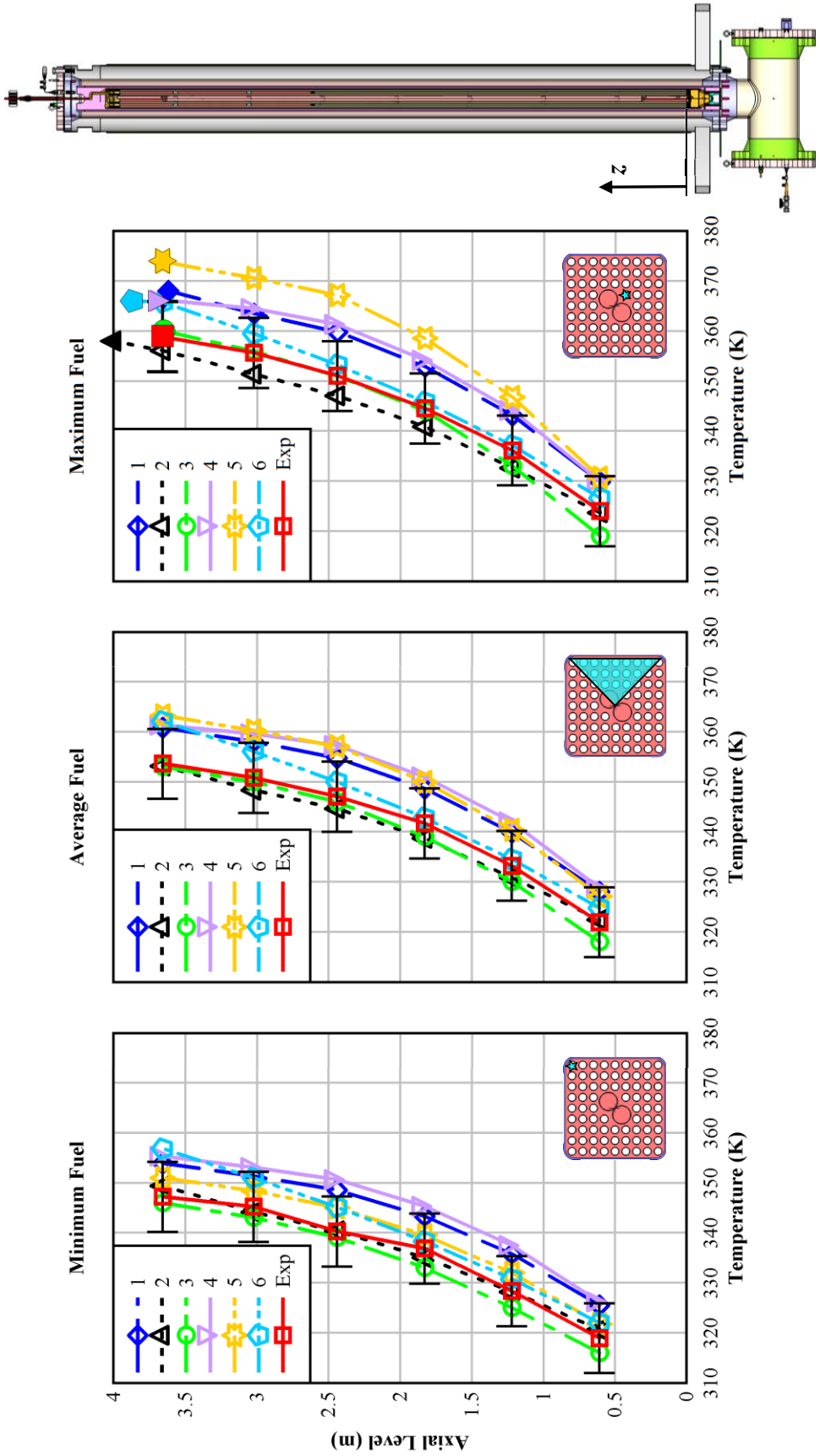

Figure 3.4 DCS fuel assembly axial temperature profile comparisons between experiment and model results for the 0.5 kW, 800 kPa test case. Peak cladding temperatures and their axial locations are represented by the large symbols in the maximum fuel temperature profile.

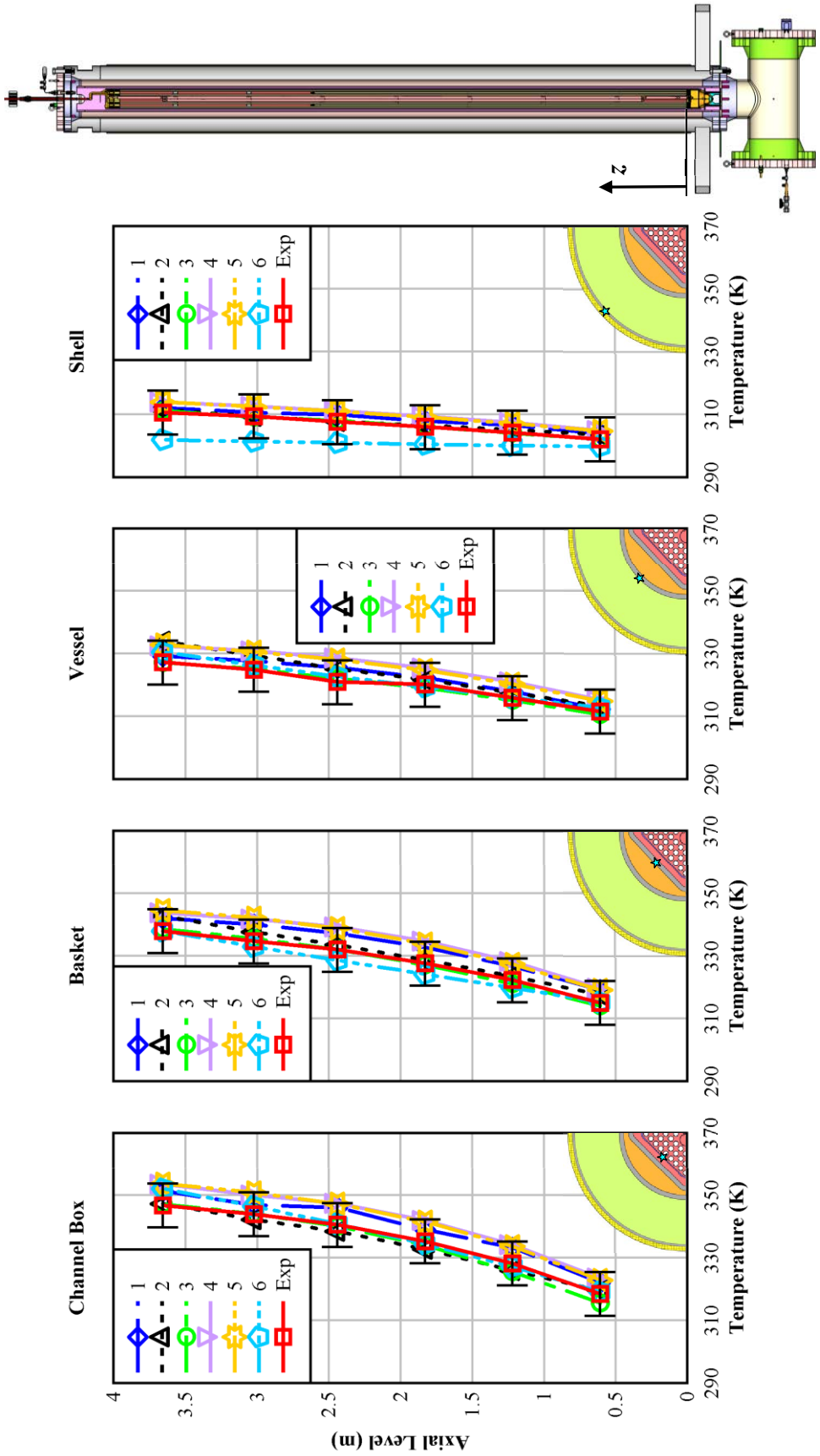

Figure 3.5 DCS structure axial temperature profile comparisons between experiment and model results for the 0.5 kW, 800 kPa test case.

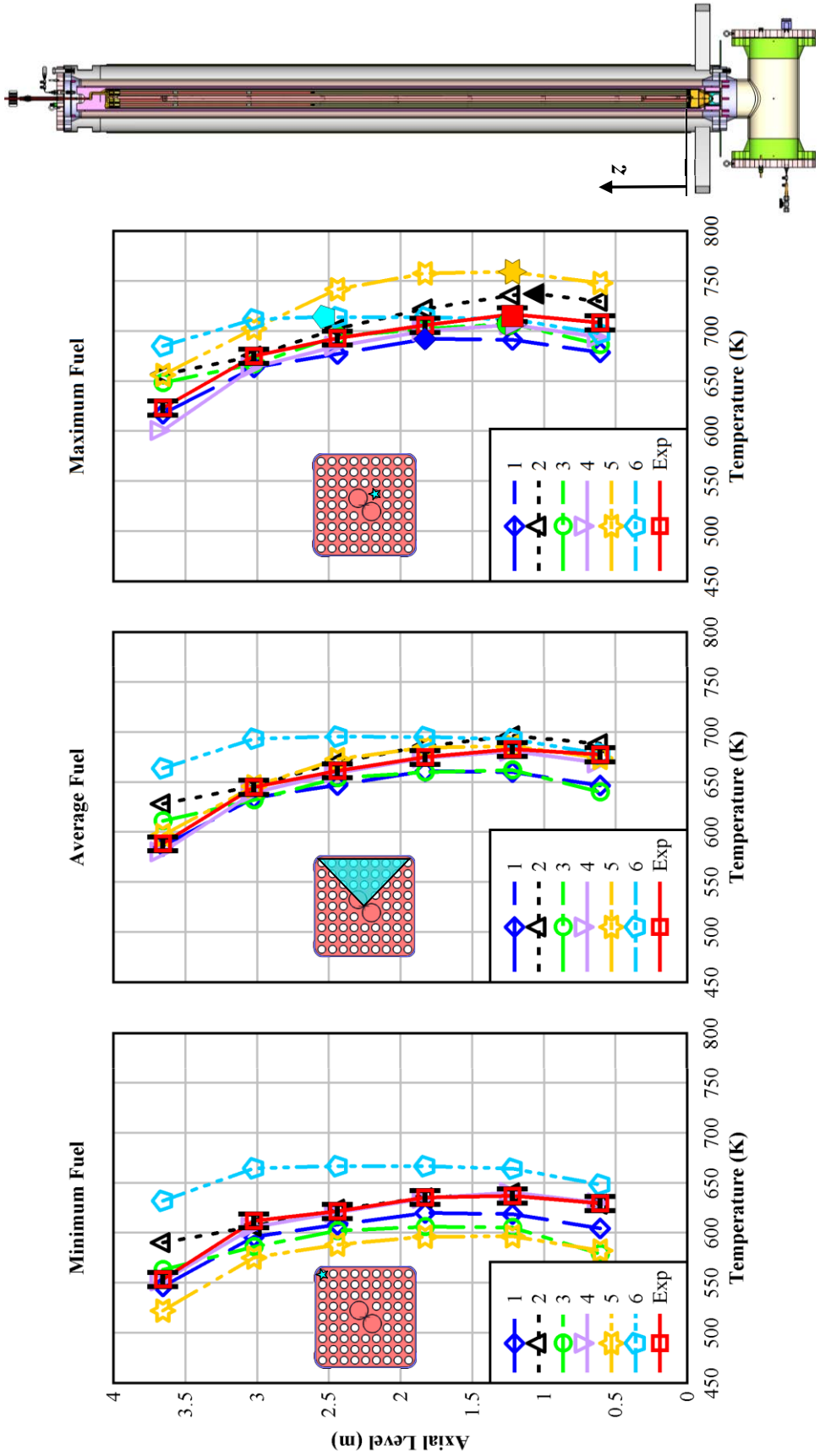

Figure 3.6 DCS fuel assembly axial temperature profile comparisons between experiment and model results for the 5 kW, 100 kPa test case. Peak cladding temperatures and their axial locations are represented by the large symbols in the maximum fuel temperature profile.

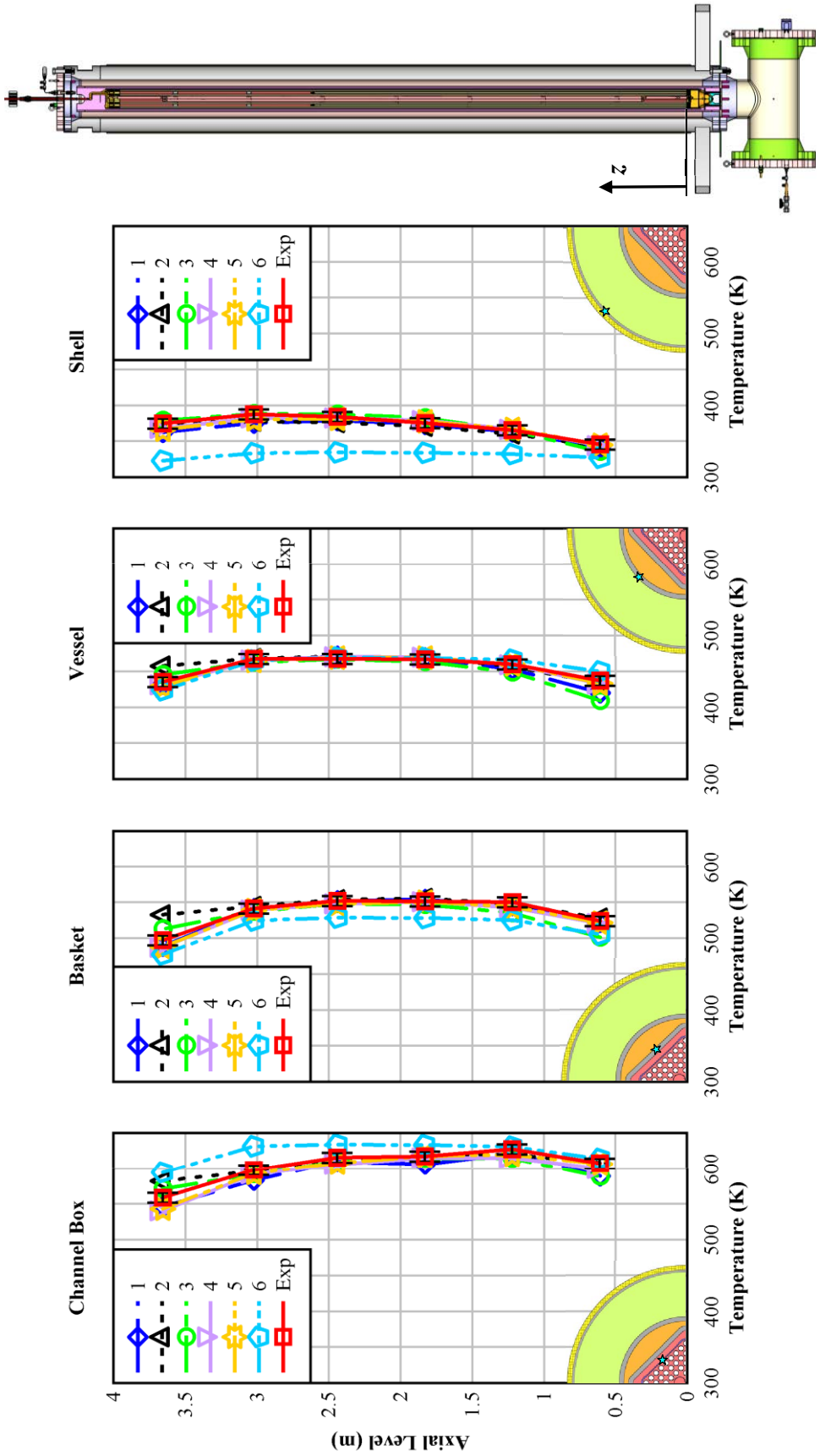

Figure 3.7 DCS structure axial temperature profile comparisons between experiment and model results for the 5 kW, 100 kPa test case.

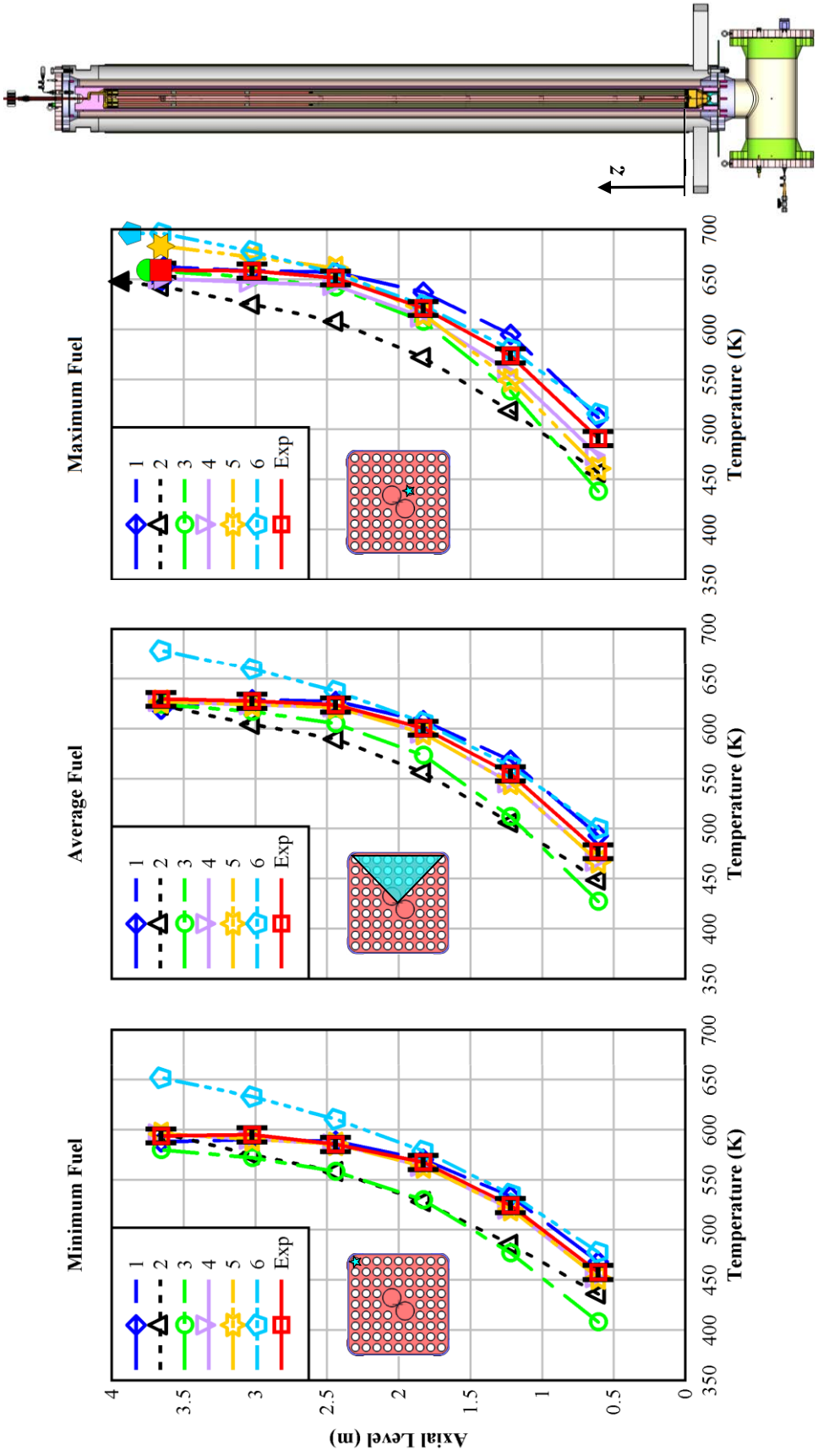

Figure 3.8 DCS fuel assembly axial temperature profile comparisons between experiment and model results for the 5 kW, 800 kPa test case. Peak cladding temperatures and their axial locations are represented by the large symbols in the maximum fuel temperature profile.

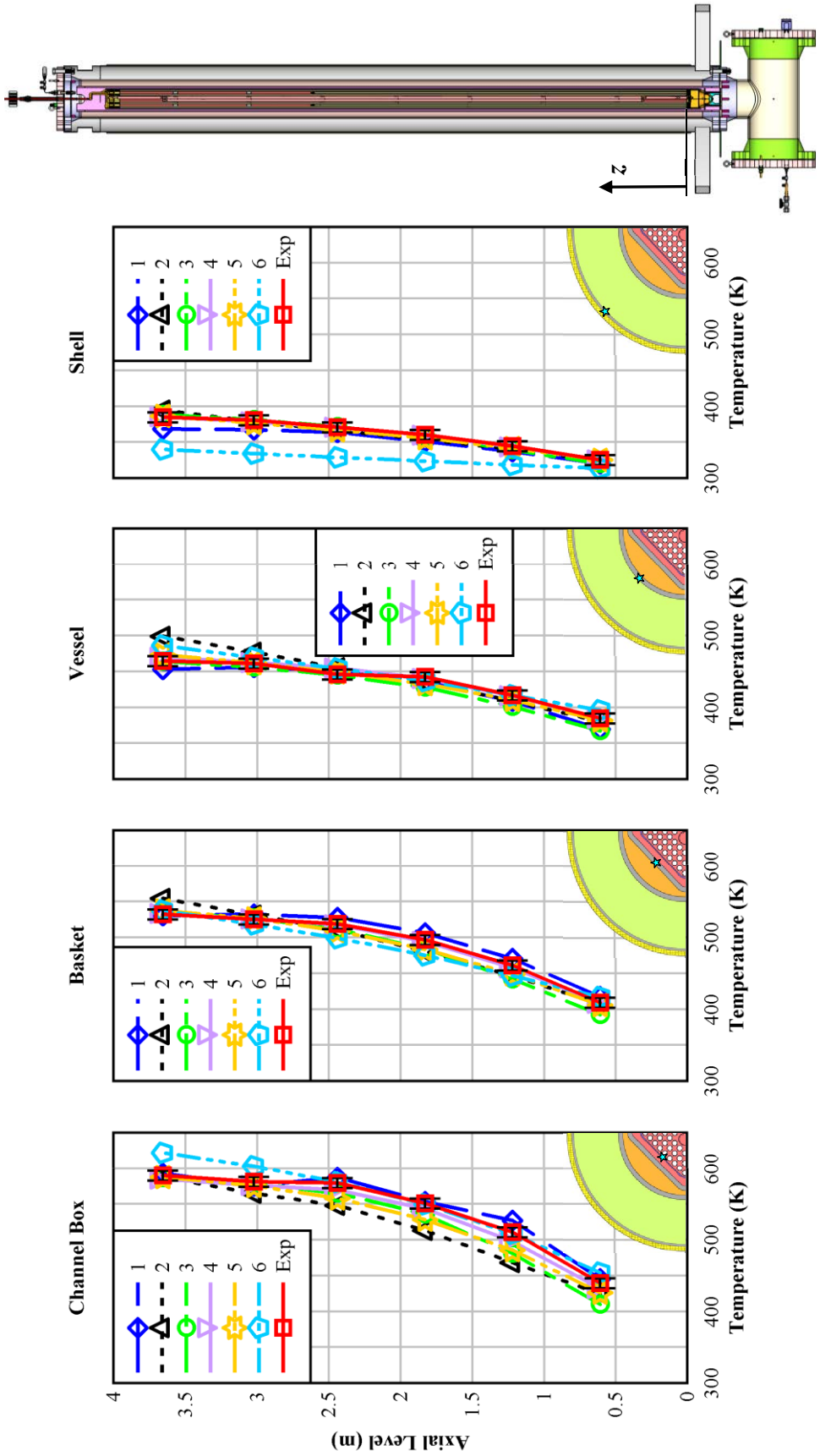

Figure 3.9 DCS structure axial temperature profile comparisons between experiment and model results for the 5 kW, 800 kPa test case.

Transverse temperature profiles of the DCS system from the experiments and the models at the peak cladding temperature locations for the four test matrix cases are shown in Figure 3.10 through Figure 3.13. The inset in these plots shows a cross-section of the fuel assembly and the DCS outer components to the pressure vessel wall. Here, the blue stars show the six transverse locations where experimental temperature data were obtained. Once again, the error bars correspond to the experimental error, defined as 1% of the maximum observed PCT (715 K) or ±7 K.

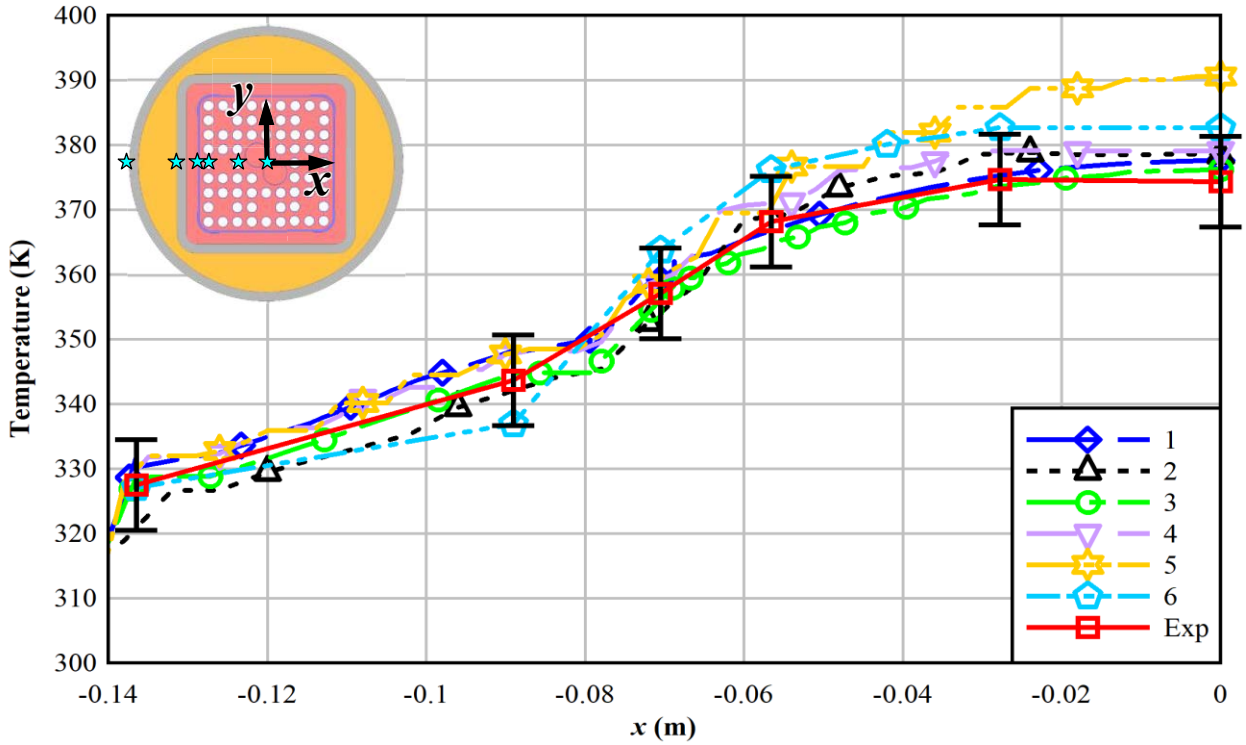

Figure 3.10 DCS transverse temperature profile comparisons between experiment and model results at axial level 1.829 m for the 0.5 kW, 100 kPa test case.

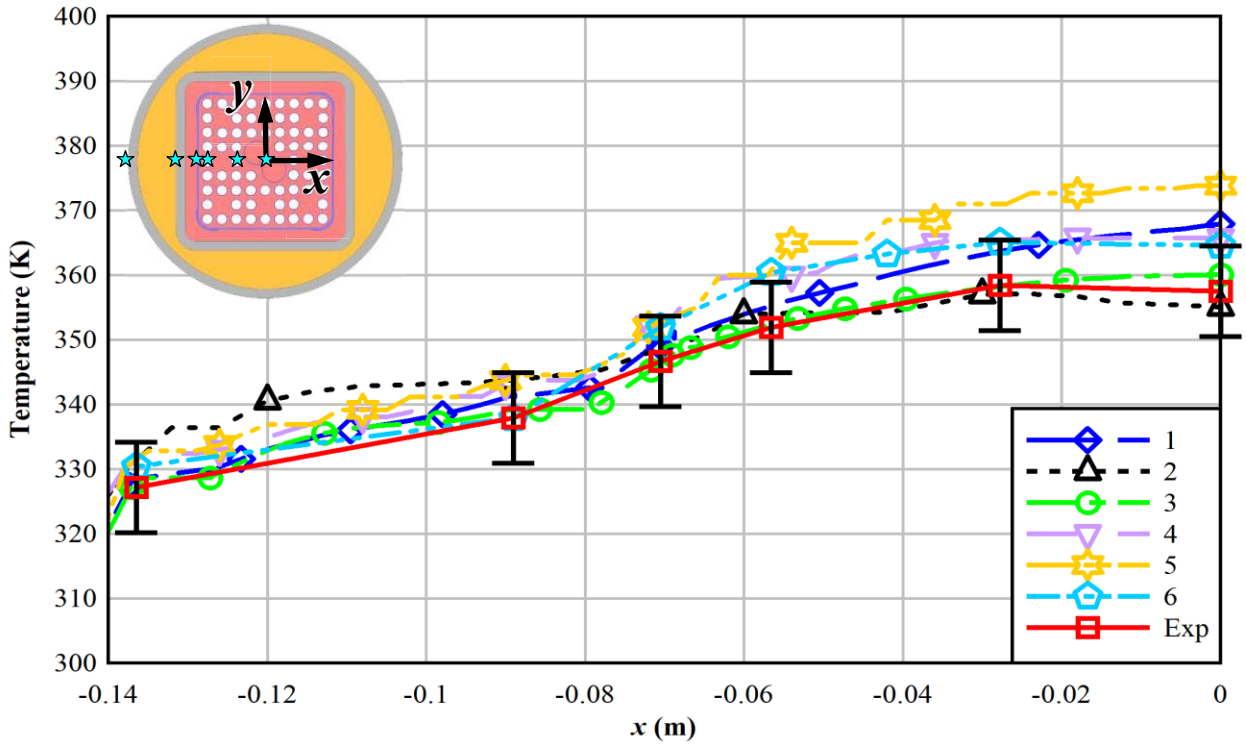

Figure 3.11 **DCS transverse temperature profile comparisons between experiment and model results at axial level 3.658 m for the 0.5 kW, 800 kPa test case.**

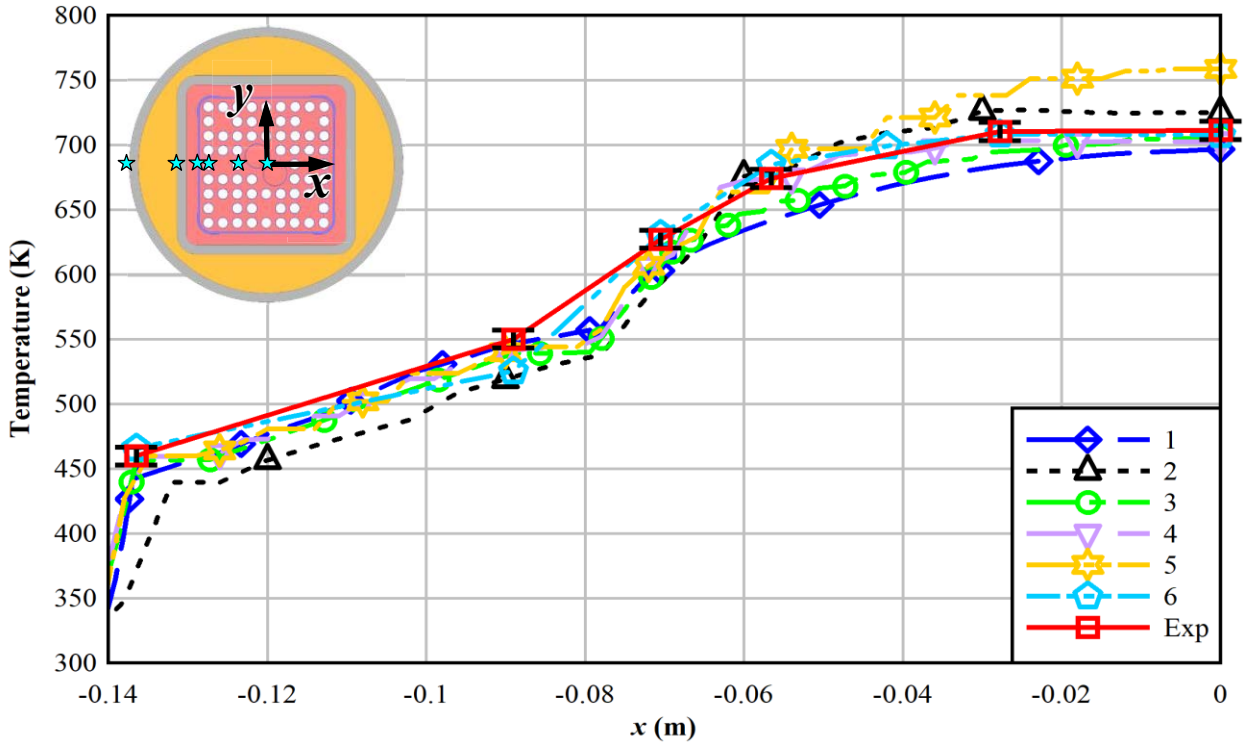

Figure 3.12 **DCS transverse temperature profile comparisons between experiment and model results at axial level 1.219 m for the 5 kW, 100 kPa test case.**

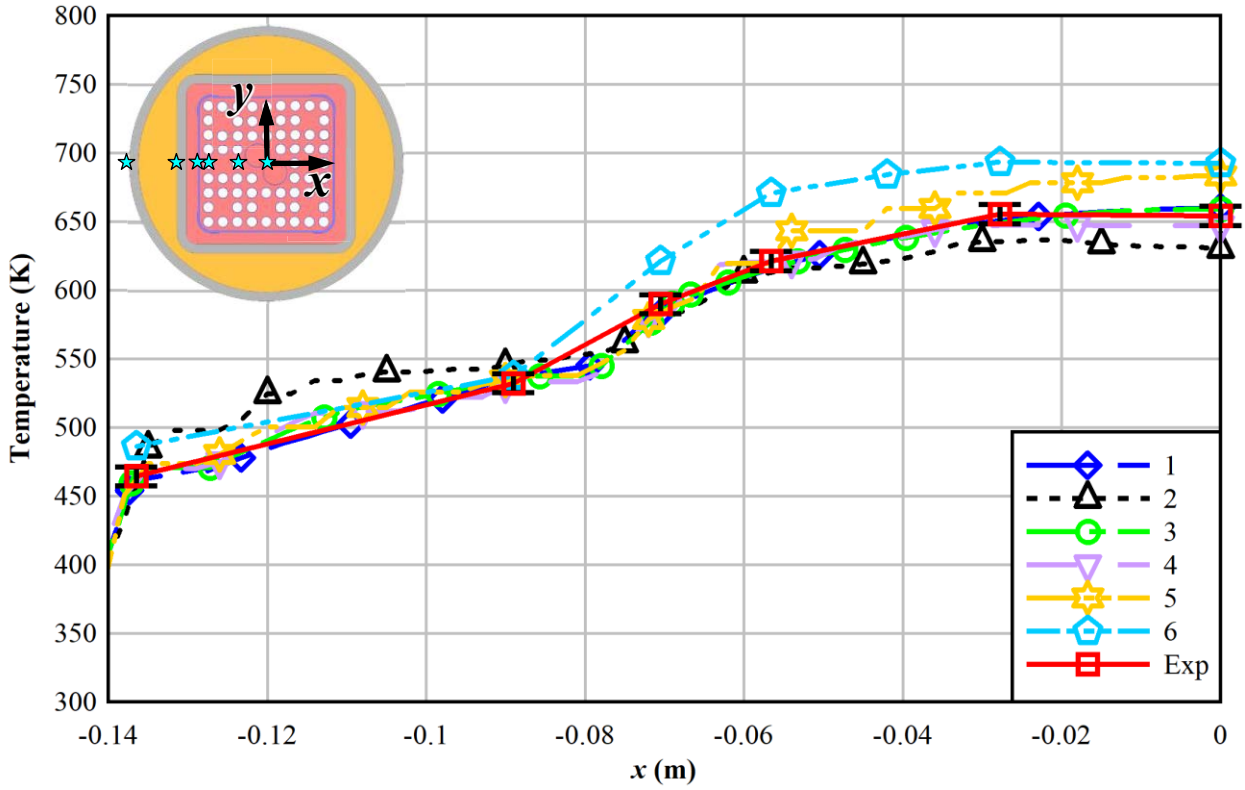

Figure 3.13 DCS transverse temperature profile comparisons between experiment and model results at axial level 3.658 m for the 5 kW, 800 kPa test case.

3.2.1 Root Mean Square Error Comparisons

The error found in the comparison of modeling results versus experimental data for the target variables (PCT, average fuel axial temperature across six axial levels, transverse temperature across the PCT locations for the four test cases, and air mass flow rate) is calculated as the difference in experimental and modeling results divided by the experimental result. Equation 3-1 expresses this, where ε_x is the error in the target variable x and x_E and x_M refer to the experimental and model results, respectively:

$$\varepsilon_x = \frac{x_M - x_E}{x_E} \tag{3-1}$$

Calculation of the root mean square (RMS) error values for the target variables quantifies the closeness of fit of each model's results to the experimental data. Table 3.2 shows the RMS error calculation for the PCT, while Table 3.4 shows the RMS calculations for the average fuel temperature error between experimental data and model results across six axial levels for all test cases. Here, the six axial levels of interest are 0.610 m, 1.219 m, 1.829 m, 2.438 m, 3.023 m, and 3.658 m, and $\overline{T}_i$ represents the mass-weighted average fuel temperature at axial level *i*. Table 3.6 shows the RMS calculations for the transverse temperature errors – these values are obtained from the comparison of model results to experimentally determined temperatures at six radial locations along the peak cladding temperature axial levels for each test case. Here, the radial locations of interest at these PCT axial levels, defining x = 0 m at the center of the fuel assembly, are x = 0 m, x = -0.0278 m, x = -0.0566 m, x = -0.0705 m, x = -0.089 m, and x = -0.1365 m (refer to the locations of the blue stars in the inset of Figure 3.10). Table 3.8 shows the RMS calculations for the air mass flow rate errors.

Experimental and modeling uncertainties in the error of the target variables of interest are accounted for in this analysis. The uncertainty is calculated using Equation 3-2:

$$U_{\varepsilon_x} = \sqrt{\left(\frac{\partial \varepsilon_x}{\partial x_E}\right)^2 \cdot U_{x_E}^2 + \left(\frac{\partial \varepsilon_x}{\partial x_M}\right)^2 \cdot U_{x_M}^2} \quad (3\text{-}2)$$

Here, the uncertainty in the error U_{ε_x} is found by taking the square root of the sum of the squares of two terms – the partial derivative of the error with respect to the experimental result multiplied by the experimental expanded uncertainty U_{x_E}, and the partial derivative of the error with respect to the modeling result multiplied by the model expanded uncertainty U_{x_M}.

The maximum experimental expanded uncertainties for temperature and air mass flow rate are 7 K and 1.5E-3 kg/s, respectively [Durbin and Lindgren, 2018]. NRC conducted an uncertainty analysis for the peak cladding temperature and air mass flow rate (see Table A.1 in Appendix A), yielding maximum model expanded uncertainties for temperature and air mass flow rate of 11.7 K and 1.24E-3 kg/s, respectively. These numerical uncertainties are assumed to be representative of the other models – this assumption may be reasonable for the CFD results, but it may not necessarily apply to the COBRA results. The assumption is also limited in scope, but it was made based on currently available information.

Table 3.3, Table 3.5, Table 3.7, and Table 3.9 show the error normalized by the expanded (95%) error uncertainty of the PCTs, average fuel axial temperatures across six axial levels, transverse temperatures across the PCT locations for the four test cases, and air mass flow rates, respectively (as calculated by Equation 3-2). These tables provide additional quantification of the closeness of fit of each model's results to the experimental data by taking the expanded uncertainty into account. The tables are heat mapped according to this expanded uncertainty, with green corresponding to less than one standard error, yellow corresponding to one standard error, and red corresponding to two standard errors (equivalent to the expanded error).

Table 3.2 Peak cladding temperature error.

Conditions \ Model		1	2	3	4	5	6
Power (kW)	Pressure (kPa)	$(T_{Model}-T_{Exp})/T_{Exp}$					
0.5	100	0.0081	0.0120	0.0011	0.0118	0.0399	0.0224
0.5	800	0.0258	-0.0019	0.0036	0.0208	0.0420	0.0203
5	100	-0.0328	0.0305	-0.0116	-0.0126	0.0605	-0.0019
5	800	0.0050	-0.0159	0.0004	-0.0128	0.0374	0.0566
RMS[Error(PCT)]		0.021	0.018	0.006	0.015	0.046	0.032

Table 3.3 Peak cladding temperature error normalized by the expanded uncertainty.

Conditions \ Model		1	2	3	4	5	6
Power (kW)	Pressure (kPa)	$Error(PCT)/U_{Error}(PCT)$					
0.5	100	0.22	0.33	0.03	0.32	1.09	0.61
0.5	800	0.68	0.05	0.09	0.54	1.09	0.53
5	100	1.74	1.59	0.61	0.66	3.12	0.10
5	800	0.24	0.77	0.02	0.62	1.79	2.69
$RMS[Error(PCT)/U_{Error}(PCT)]$		0.95	0.90	0.31	0.55	1.96	1.41

Table 3.4 RMS of average fuel temperature error across six axial levels.

Conditions \ Model		1	2	3	4	5	6
Power (kW)	Pressure (kPa)	$\sqrt{\sum_{i=1}^{6}\frac{\left[(\bar{T}_{Model,i}-\bar{T}_{Exp,i})/\bar{T}_{Exp,i}\right]^2}{6}}$, where i denotes different axial levels					
0.5	100	0.0044	0.0187	0.0102	0.0112	0.0155	0.0366
0.5	800	0.0204	0.0062	0.0074	0.0253	0.0245	0.0127
5	100	0.0271	0.0306	0.0327	0.0086	0.0113	0.0655
5	800	0.0188	0.0593	0.0581	0.0118	0.0118	0.0445
$RMS[Error(\bar{T}(z))]$		0.020	0.035	0.034	0.016	0.017	0.044

Table 3.5 RMS of average fuel temperature error across six axial levels normalized by the expanded uncertainty.

Conditions \ Model		1	2	3	4	5	6
Power (kW)	Pressure (kPa)	$Error(\bar{T}(z))/U_{Error}(\bar{T}(z))$					
0.5	100	0.12	0.49	0.27	0.30	0.41	0.97
0.5	800	0.51	0.16	0.18	0.63	0.61	0.32
5	100	1.30	0.36	1.57	0.41	0.54	3.09
5	800	0.79	2.55	2.49	0.50	0.50	1.86
$RMS[Error(\bar{T}(z))/U_{Error}(\bar{T}(z))]$		0.81	1.31	1.48	0.48	0.52	1.87

Table 3.6 Transverse temperature error.

Conditions \ Model		1	2	3	4	5	6
Power (kW)	Pressure (kPa)	$\sqrt{\sum_{j=1}^{6}\frac{\left[(T(x)_{Model,j}-T(x)_{Exp,j})/T(x)_{Exp,j}\right]^2}{6}}$, where j denotes different radial locations					
0.5	100	0.0096	0.0069	0.0047	0.0114	0.0252	0.0190
0.5	800	0.0155	0.0151	0.0038	0.0199	0.0310	0.0166
5	100	0.0273	0.0274	0.0206	0.0115	0.0352	0.0206
5	800	0.0077	0.0303	0.0094	0.0089	0.0267	0.0551
RMS[Error(T(x)]		0.017	0.022	0.012	0.014	0.030	0.032

Table 3.7 Transverse temperature error normalized by the expanded uncertainty.

Conditions \ Model		1	2	3	4	5	6
Power (kW)	Pressure (kPa)	Error(T(x))/U_{Error}(T(x))					
0.5	100	0.25	0.18	0.12	0.30	0.65	0.49
0.5	800	0.39	0.38	0.10	0.50	0.78	0.42
5	100	1.20	1.21	0.91	0.51	1.54	0.90
5	800	0.32	1.27	0.39	0.37	1.12	2.28
RMS[Error(T(x))/U_{Error}(T(x))]		0.66	0.90	0.50	0.43	1.08	1.27

Table 3.8 Air mass flow rate error.

Conditions \ Model		1	2	3	4	5	6
Power (kW)	Pressure (kPa)	$(\dot{m}_{Model}-\dot{m}_{Exp})/\dot{m}_{Exp}$					
0.5	100	0.0062	-0.1872	-0.0229	-0.0860	-0.0934	0.5455
0.5	800	0.0169	0.1384	-0.0102	-0.0669	-0.0830	0.7919
5	100	-0.0121	-0.0684	0.0049	-0.0079	-0.0096	-0.1408
5	800	-0.0144	-0.0421	-0.0258	-0.0406	-0.0493	-0.1022
RMS[Error($\dot{m}$)]		0.013	0.123	0.018	0.058	0.067	0.489

Table 3.9 Air mass flow rate error normalized by the expanded uncertainty.

Conditions \ Model		1	2	3	4	5	6
Power (kW)	Pressure (kPa)	Error($\dot{m}$)/U_{Error}($\dot{m}$)					
0.5	100	0.08	2.84	0.32	1.23	1.34	5.48
0.5	800	0.19	1.45	0.12	0.79	0.99	5.91
5	100	0.43	2.52	0.17	0.28	0.34	5.41
5	800	0.47	1.39	0.84	1.34	1.63	3.50
RMS[Error($\dot{m}$)/U_{Error}($\dot{m}$)]		0.33	2.15	0.46	1.00	1.18	5.16

Table 3.10 provides a combined RMS error calculation for each model across the four target variables – the PCT, the average fuel axial temperature across six axial levels, the transverse temperature across the PCT locations for the four test cases, and the air mass flow rate. These combined RMS errors can be used to determine how well each model's results fit with the overall experimental results. However, these RMS errors do not take uncertainty into account.

RMS calculations were performed for the uncertainties using the same methodology as was used for the errors. Table 3.11 provides a combined RMS error calculation for each target variable that is normalized by the RMS expanded uncertainties. The heat mapping follows the same rules as the previous normalized error tables. This table provides an additional measure of the goodness of fit of the modeling results to the experimental data by taking the expanded uncertainty into account.

Table 3.10 Combined PCT, average fuel temperature, transverse temperature, and air mass flow rate RMS error.

Model / RMS Error	1	2	3	4	5	6
PCT	0.021	0.018	0.006	0.015	0.046	0.032
$\overline{T}(z)$	0.020	0.035	0.034	0.016	0.017	0.044
$T(x)$	0.017	0.022	0.012	0.014	0.030	0.032
$\dot{m}$	0.013	0.123	0.018	0.058	0.067	0.489
Combined	0.018	0.066	0.020	0.032	0.044	0.246

Table 3.11 Combined PCT, average fuel temperature, transverse temperature, and air mass flow rate RMS error normalized by the expanded uncertainty.

Model / Normalized RMS Error	1	2	3	4	5	6
PCT	0.70	0.60	0.20	0.50	1.53	1.07
$\overline{T}(z)$	0.63	1.11	1.08	0.50	0.53	1.38
$T(x)$	0.53	0.69	0.37	0.44	0.93	1.00
$\dot{m}$	0.21	2.00	0.30	0.99	1.15	5.71
Combined	0.55	1.23	0.60	0.65	1.10	3.02

4 SUMMARY

In this validation exercise, five institutions (NRC, PNNL, CIEMAT, and ENUSA-UPM) provided their own unique approaches to capturing the temperature profiles and air mass flow rates within the BWR dry cask simulator in the aboveground configuration. For these comparisons, four test cases of the vertical, aboveground dry cask simulator were considered, defined by two independent variables – either 0.5 kW or 5 kW fuel assembly decay heat, and either 100 kPa or 800 kPa internal helium pressure. For all cases, the modelers obtained the peak cladding temperatures, the average fuel axial temperature profiles, the transverse temperatures across the PCT locations for the four test cases, and the air mass flow rates external to the assembly. The different modeling codes used by each institution encompassed a variety of computational approaches to determining these target variables – these approaches were characterized mainly by the software used (ANSYS FLUENT, STAR-CCM+, or COBRA-SFS) and the use of either porous media or explicit fuel models to describe the dry cask simulator.

The plots provided in Chapter 3 show the axial and transverse temperature profiles obtained from the dry cask simulator experiments in the aboveground configuration and the corresponding models used to describe the thermal-hydraulic behavior of this system. The tables provided in Chapter 3 illustrate the closeness of fit of the model data to the experiment data through root mean square calculations of the error in PCTs, average fuel temperatures across six axial levels, transverse temperatures across the PCT locations for the four test cases, and air mass flow rates for all test cases.

The axial temperature profiles for the DCS structures provided by the models trend closer to the experimental data than the axial temperature profiles for the fuel assembly in all four test cases. Further work is needed to determine the reasons for these trends. However, one immediate observation noted was that the temperature profiles moving outward from the fuel assembly to the structures approach the same ambient temperatures.

Based on the combined RMS error calculations (Table 3.10), model 1 and model 3 offered the results that best fit overall to the experimental data, with the models generating combined RMS error values of 0.018 and 0.020, respectively. Model 4 is the next closest, generating a combined RMS error value of 0.032. Models 5, 2, and 6 follow, with combined RMS error values of 0.044, 0.066, and 0.246, respectively. The model performance is consistent when considering the combined RMS errors normalized by the RMS expanded uncertainty (Table 3.11). Model 1 and model 3 show normalized RMS errors of 0.55 and 0.60, respectively. Model 4 generated a combined RMS normalized error of 0.65, while models 5, 2, and 6 show combined RMS normalized errors of 1.10, 1.23, and 3.02, respectively.

The peak cladding temperature is typically the most important target variable for cask performance, and all models capture the PCTs within 5% RMS error. The average fuel axial temperatures and the transverse temperatures were also captured within 5% RMS error. Only model 1 and model 3 capture the air mass flow rates within 5% RMS error.

As a reminder, even-numbered models use explicit fuel representations, while odd-numbered models represent the fuel as a porous media. Since model 3 and model 4 show similar RMS errors when considering the combined result of all target variables, it can be concluded that the porous media fuel representation can achieve modeling calculation results of peak cladding temperatures, average fuel temperatures, transverse temperatures, and air mass flow rates that are comparable to explicit fuel representation modeling results.

4.1 Recommendations for Future Validation Studies

This validation study was valuable in identifying several metrics and methods for analyzing the goodness of fit for different thermal-hydraulic models for dry storage applications. As part of these results, recommendations were recorded to improve future efforts. Key among these observations were the following.

1. Numerical uncertainty analyses: Future modeling efforts should include a rigorous estimation of modeling uncertainty to enhance interpretation of the results.
2. Sensitivity analyses: Input parameters and choice of closure models should be explored and documented to gain a greater insight into model performance. These observations should be used to influence best practice guidelines.
3. Baseline numerical case: A single, baseline case with prescribed grid sizes and closure models should be performed by each modeling team to provide a more direct comparison of the underlying modeling physics. It is recognized that this recommendation is more applicable to CFD submissions and is likely not possible for lumped-parameter or subchannel models.

5 REFERENCES

Bates, J.M., "Single PWR Spent Fuel Assembly Heat Transfer Data for Computer Code Evaluations," Pacific Northwest Laboratory, Richland, Washington, PNL-5571, January 1986.

Creer, J.M., T.E. Michener, M.A. McKinnon, J.E. Tanner, E.R. Gilbert, R.L. Goodman, "The TN-24P PWR Spent Fuel Storage Cask: Testing and Analyses," EPRI NP-5128 Proj. 2406-4, PNL-6054, Pacific Northwest Laboratory, Richland, Washington, April 1987.

Cuta, J.M. and H.E. Adkins, "Preliminary Thermal Modeling of Hi-Storm 100 Storage Modules at Diablo Canyon Power Plant ISFSI," Research Report FCRD-UFD-2014-000505, April 2014.

Durbin, S.G., E.R. Lindgren, A. Zigh, and J. Solis, "Description of Dry Cask Simulator for Measuring Internal and External Thermal-Hydraulic Performance," SAND2016-0176C, Trans. Am. Nucl. Soc., New Orleans, LA, June 2016.

Durbin, S.G. and E.R. Lindgren, "Thermal-Hydraulic Experiments Using a Dry Cask Simulator," NUREG/CR-7250, Sandia National Laboratories, Albuquerque, New Mexico, October 2018.

Dziadosz, D., E.V. Moore, J.M. Creer, R.A. McCann, M.A. McKinnon, J.E. Tanner, E.R. Gilbert, R.L. Goodman, D.H. Schoonen, M. Jensen, and C. Mullen, "The Castor-V/21 PWR Spent-Fuel Storage Cask: Testing and Analyses," Electrical Power Research Institute, EPRI NP-4887, Project 2406-4, PNL-5917, Pacific Northwest Laboratory, Richland, Washington, November 1986.

Irino, M., M. Oohashi, T. Irie, and T. Nishikawa, "Study on Surface Temperatures of Fuel Pins in Spent Fuel Dry Shipping/Storage Casks," IAEA-SM-286/139P, in Proceedings of Packaging and Transportation of Radioactive Materials (PATRAM '86), Volume 2, p. 585, International Atomic Energy Agency Vienna, 1987.

Fort, J.A., D.J. Richmond, J.M. Cuta, and S.R. Suffield, "Thermal Modeling of TN-32B CASK for High Burnup Spent Fuel Data Project," PNNL-24549 Rev. 2, Pacific Northwest National Laboratory, Richland, Washington, September 2018.

Li, J. and Y.Y. Liu, "Thermal Modeling of a Vertical Dry Storage Cask for Used Nuclear Fuel," Nuclear Engineering and Design, Volume 301, p. 74-88, Argonne National Laboratory, Lemont, Illinois, January 2016.

Lindgren, E.R. and S.G. Durbin, "Characterization of Thermal-Hydraulic and Ignition Phenomena in Prototypic, Full-Length Boiling Water Reactor Spent Fuel Pool Assemblies after a Complete Loss-of-Coolant Accident," SAND2007-2270, Sandia National Laboratories, Albuquerque, New Mexico, April 2007.

Lindgren, E.R. and S.G. Durbin, "Materials and Dimensional Reference Handbook for the Boiling Water Reactor Dry Cask Simulator," SAND2017-13058R, Sandia National Laboratories, Albuquerque, New Mexico, November 2017

Lombardo, N.J., T.E. Michener, C.L. Wheeler, and D.R. Rector, "Cobra-SFS Predictions of Single Assembly Spent Fuel Heat Transfer Data," PNL-5781, Pacific Northwest Laboratory, Richland, Washington, April 1986.

McKinnon, M.A., J.W. Doman, J.E. Tanner, R.J. Guenther, J.M. Creer and C.E. King, "BWR Spent Fuel Storage Cask Performance Test, Volume 1, Cask Handling Experience and Decay Heat, Heat Transfer, and Shielding Data," PNL-5777 Vol. 1, Pacific Northwest Laboratory, Richland, Washington, February 1986.

McKinnon, M.A., J.M. Creer, C. L. Wheeler, J.E. Tanner, E.R. Gilbert, R.L. Goodman, D.P. Batala, D.A. Dziadosz, E.V. Moore, D.H. Schoonen, M.F. Jensen, and J.H. Browder, "The MC-10 PWR Spent Fuel Storage Cask: Testing and Analysis," EPRI NP-5268, PNL-6139, Pacific Northwest Laboratory, Richland, Washington, July 1987.

McKinnon, M.A., T.E. Michener, M.F. Jensen, G.R. Rodman, "Testing and Analyses of the TN-24P Spent Fuel Dry Storage Cask Loaded with Consolidated Fuel," EPRI NP-6191 Project 2813-16, PNL-6631, Pacific Northwest Laboratory, Richland, Washington, February 1989.

McKinnon, M.A., R.E. Dodge, R.C. Schmitt, L.E. Eslinger, & G. Dineen, "Performance Testing and Analyses of the VSC-17 Ventilated Concrete Cask," EPRI-TR-100305, Electric Power Research Institute, Palo Alto, California, May 1992.

Rector, D.R., T.E. Michener, and J.M. Cuta, "Verification and Validation of COBRA-SFS Transient Analysis Capability," PNNL-11883, Pacific Northwest National Laboratory, Richland, Washington, May 1998.

Waldrop, K. and J. Kessler, "Update on in-service inspections of stainless steel dry storage canisters," Document ML14052A430 (slides), NEI-NRC Meeting on Spent Fuel Storage Cask Material Degradation, January 2014.

U.S. Nuclear Regulatory Commission, Interim Staff Guidance-11, Revision 3, "Cladding Considerations for the Transportation and Storage of Spent Fuel," NRC Spent Fuel Project Office, November 2003.

Zigh, A., S. Gonzalez, J. Solis, S.G. Durbin, and E.R. Lindgren, "Validation of the Computational Fluid Dynamics Method Using the Aboveground Configuration of the Dry Cask Simulator," SAND2017-6104C, Trans. Am. Nucl. Soc., San Francisco, CA, June 2017.

Zigh, A., and J. Solis. "Computational Fluid Dynamics Best Practice Guidelines for Dry Cask Applications," U.S. Nuclear Regulatory Commission, NUREG-2152, Washington, DC, March 2013.

Zigh, A., and J. Solis. "Validation of Computational Fluid Dynamics Methods Using Prototypic Light Water Reactor Spent Fuel Assembly Thermal-Hydraulic Data," U.S. Nuclear Regulatory Commission, NUREG-2208, Washington, DC, March 2017.

APPENDIX A – NRC MODEL INFORMATION

ANSYS/Fluent 18 was used to model the response of the DCS in an aboveground configuration, similar to earlier simulations for prototypic cask systems [Zigh and Solis, 2016]. The model geometry was built and created using Gambit version 2.4. The same software was also used to create the mesh. The mesh was created using the best practice guideline NUREG [Zigh and Solis, 2013].

A.1 Model Description

A.1.1 Representation of Fuel Assembly

To model the fuel region, porous media was used as all dry cask applicants favor the use of the porous model or media method, because it simplifies the configuration and saves on processing time. The use of the porous media involves representing the absence of components with an equivalent frictional and inertial hydraulic loss. An equivalent thermal conductivity representing both radiation and conduction inside the assembly along with an equivalent density and specific heat capacity were used. In NUREG-2208, "Validation of Computational Fluid Dynamics Methods Using Prototypic Light Water Reactor Spent Fuel Assembly Thermal-Hydraulic Data" [Zigh and Gonzalez, 2017], the use of porous media was validated and shown to give comparable results as in the detailed model where fuel rods and grid spacers were represented.

The combination of radiation and conduction heat transfer within the assembly is represented by an effective thermal conductivity (k_{eff}). To accomplish this task, a two-dimensional (2D) CFD model representing the detailed cross section of an assembly explicitly showing fuel rods was used to obtain k_{eff} for different temperature boundary conditions. Radial and axial components of the effective conductivity were calculated and used as input for the porous media as a function of temperature. The TRW Environmental Safety Systems, Inc. report, "Spent Nuclear Fuel Effective Thermal Conductivity Report," [TRW Environmental Safety Systems, Inc., 1996] describes the k_{eff} approach in detail. In NUREG-2008, calculations in the TRW report were confirmed using the developed model using CFD ANSYS, which was then used to obtain k_{eff} for the BWR 9×9 assembly.

A.1.2 Representation of DCS Structures

Per CFD best practice guidelines [Zigh and Solis, 2013], a hex mesh was used throughout all the control volume regions. In the air flow region, a y+ close to unity was used to appropriately use the Low Reynolds k-ε turbulence model. This turbulence model does not use wall functions to bridge the turbulence model to the wall's boundary condition of turbulent kinetic energy and its dissipation.

The conservation equations for k and ε are integrated all the way to the wall through the use of finer meshing close to the wall. CFD best practice guidelines were used for the expansion ratio for successive volume meshing and mesh skewness.

A.1.3 Approximations and Treatments

A.1.3.1 Internal Fuel Assembly and External DCS Structure Treatment

The interior helium gas was assumed to be laminar while the external air region was assumed to behave according to the Low Reynolds k-ε turbulence model using a full buoyancy effect. No wall function model was used to integrate to the wall. Second order upwind discretization was used for all the conservation equations. Radiation heat transfer was modeled using the Discrete Ordinates (DO) model using second order upwind discretization. A pressure solver was used using Semi-Implicit Method for Pressure-Linked Equations (SIMPLE) to link the conservation of momentum equation to the continuity equation. The least square cell-based method was used for gradient discretization. Body force weighting was used for pressure interpolation. The grid was refined until a grid-independent solution was obtained to minimize the discretization error.

The equivalent frictional and inertial hydraulic losses were obtained based on previous analysis documented in NUREG-2208 [Zigh and Gonzalez, 2017]. As shown in the NUREG, the initial guess of the friction factor was obtained from the isothermal pressure drop method obtained either from the experiment or the isothermal shear stress method. The final friction factor was obtained by comparing the peak cladding temperature (PCT) values between the porous and the detailed models.

A.1.3.2 Input Parameters

Both helium and air were modeled using the ideal gas law. Transient and steady solutions were obtained. Temperature dependence for solid materials and fluid were implemented in the model. Material properties including density, thermal conductivity, weight, specific heat and emissivity were obtained from the "Materials and Dimensional Reference Handbook for the Boiling Water Reactor Dry Cask Simulator" [Lindgren and Durbin, 2017].

The equivalent density and equivalent heat capacity were calculated based on the area ratio as a function of temperature. Further details about how to obtain the proper porous media input are explained in NUREG-2208 [Zigh and Gonzalez, 2017].

A.1.3.3 Initial and Boundary Conditions

The boundary conditions and models input used in the CFD model were representative of those present during the experiment – namely, a 300 K ambient temperature and an 84 kPa ambient air pressure. The regulated measured pressure for the helium inside the canister was patched inside the helium flow. For the convection to the outside of the cask, a natural turbulent heat transfer coefficient was used at the outside surface of the cask. The inlet flow straighteners at the inlet duct were modeled as porous media. Equivalent frictional and inertial losses used in the porous model were calculated using existing flow area contractions and expansions. The outer surfaces bounding the control volume as shown in Figure A.1 and Figure A.2 were allowed to interact with the surroundings using both convection and radiation. A natural and turbulent heat transfer correlation was used to obtain the heat transfer coefficient at these external surfaces. The correlation was implemented by linking a written subroutine to the main ANSYS/Fluent program.

A.1.3.4 Symmetry

1/4th symmetry was used for the model, as shown in Figure A.1 and Figure A.2.

Figure A.1 CFD model geometry.

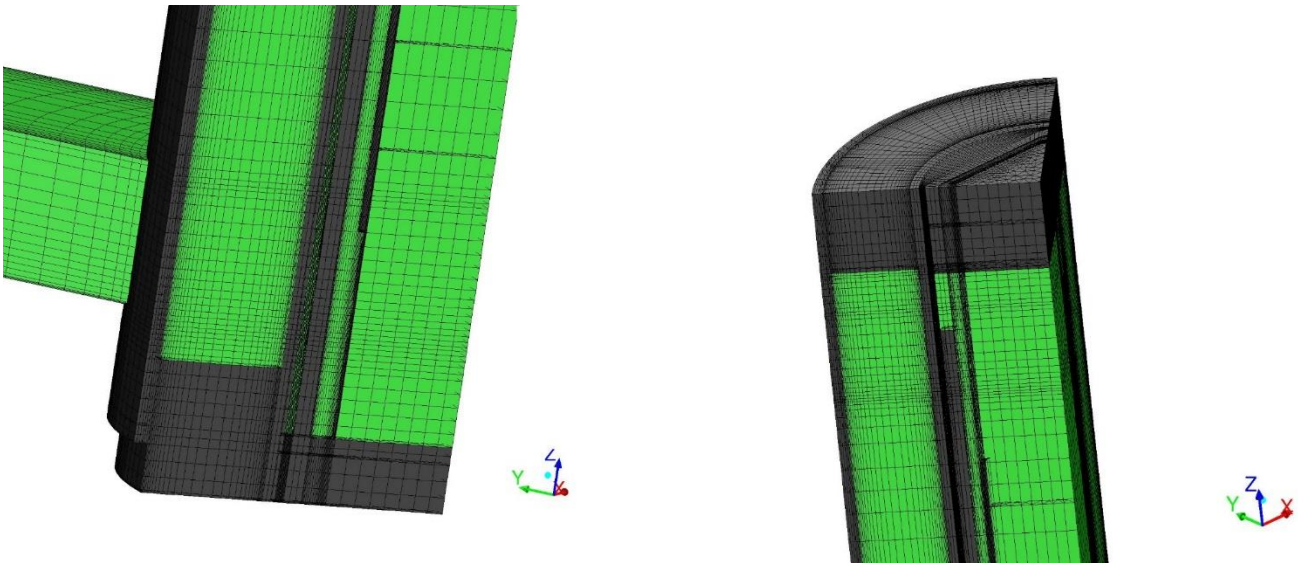

Figure A.2 CFD model mesh.

A.2 Lessons Learned

Uncertainty quantification was performed for the four test cases using ASME V&V 20-2009 [ASME, 2009]. The resulting calculations of the uncertainty quantification for the PCT and air mass flow rate are shown in Table A.1. In this table, "u" refers to the standard uncertainty.

The simulation error includes input errors as well as numerical errors. The validation error consists of input errors, numerical errors and experiment errors. The numerical error consists of convergence error, grid refinement error (i.e. solution verification) and round-off error. For detailed explanation of the method used in this calculation refer to ASME V&V 20-2009 [ASME, 2009].

Table A.1 Simulation and validation uncertainty for the PCT and air mass flow rate.

	PCT (Kelvin)		$\dot{m}_{air}$ (kg/sec)	
Case	u-simulation	u-validation	u-simulation	u-validation
5 kW, 800 kPa	10.4	12.5	1.20E-03	1.90E-03
5 kW, 100 kPa	11.7	13.6	1.24E-03	1.93E-03
0.5 kW, 800 kPa	8.0	10.6	9.31E-04	1.75E-03
0.5 kW, 100 kPa	10.3	12.4	1.03E-03	1.80E-03

As the mass flow rate and PCT values for all the cases for CFD and experiment were within the calculated uncertainty, we learned that the CFD methods that we are using and are listed in the CFD best practice guidelines, NUREG-2152 [Zigh and Solis, 2013], are correct. These modeling methods were validated and verified once again with the DCS data. We also learned to always quantify the uncertainty for the target variables (i.e. PCT and mass flow rate).

A.3 References

ASME V&V 20-2009, "Standard for Verification and Validation in Computational Fluid Dynamics and Heat Transfer," 2009.

Lindgren, E.R. and S.G. Durbin, "Materials and Dimensional Reference Handbook for the Boiling Water Reactor Dry Cask Simulator," SAND2017-13058 R, Sandia National Laboratories, Albuquerque, New Mexico, November 2017.

TRW Environmental Safety Systems, Inc., "Spent Nuclear Fuel Effective Thermal Conductivity Report," TRW Environmental Safety Systems, Inc., July 1996.

Zigh, A. and J. Solis, "Impact of Variation in Environmental Conditions on the Thermal Performance of Dry Storage Casks," Nuclear Regulatory Commission, NUREG-2174, March 2016.

Zigh, A., and J. Solis. "Computational Fluid Dynamics Best Practice Guidelines for Dry Cask Applications," U.S. Nuclear Regulatory Commission, NUREG-2152, Washington, DC, March 2013.

Zigh, A. and S. Gonzalez, "Validation of Computational Fluid Dynamics Methods Using Prototypic Light Water Reactor Spent Fuel Assembly Thermal-Hydraulic Data," Nuclear Regulatory Commission, NUREG-2208, March 2017.

APPENDIX B – PNNL MODEL INFORMATION

Three different thermal analysis models were developed to simulate the dry cask simulator (DCS). The DCS is an experiment set up to simulate a single boiling water reactor fuel assembly under a variety of heat loads and internal pressures. The models included a detailed STAR-CCM+ model with the fuel assembly and flow straightener geometry explicitly modeled, a porous STAR-CCM+ model with the fuel assembly and flow straightener geometry modeled as porous media regions with calculated effective properties, and a COBRA-SFS model. STAR-CCM+ version 13.02 was used to construct and run the STAR-CCM+ models. The models were run for a combination of low and high canister pressures (100 kPa and 800 kPa) and low and high internal heat loads (0.5 kW and 5 kW).

B.1 Model Description – Detailed STARCCM+ Model

A detailed model of the DCS was constructed using STAR-CCM+. All parts, except for the heater rods, were explicitly modeled including the flow straighteners and fuel assembly.

B.1.1 Representation of Fuel Assembly

The detailed model explicitly modeled the parts that make up the fuel region assembly, including the heater rods, water rods, fuel spacers, and tie plates. The parts in the detailed fuel assembly included the full and partial length heater rods, the tie plates, water rods, and spacers. The heater rod is made up of Incoloy cladding, MgO and Nichrome elements, and carbon steel pins. Each heater rod is modeled as a single volume in the CAD geometry and effective material properties were calculated and applied to the heater rods.

B.1.2 Representation of DCS Structures

All DCS structure parts were explicitly modeled including the flow straighteners near the inlet. The parts were meshed into regions connected by interface boundaries, resulting in a single conformal polyhedral volume mesh across all regions. Along each wall/fluid interface, the mesh contains a prism cell layer to improve the accuracy of the flow solution near the walls. The prism cell layer consists of orthogonal prismatic cells adjacent to the wall boundaries. The prism cell layer in the air region was four cells thick and two cells thick in the helium region.

B.1.3 Approximations and Treatments

B.1.3.1 Internal Fuel Assembly Treatment

A laminar flow model was applied to the internal helium region, which included flow within the fuel assembly. The Boussinesq model, which provides a buoyancy source term when there are small variations of density due to temperature variations, was applied to the helium region. Internal radiation was included in the helium gas regions and the emissivity values applied along the inner surfaces were taken from the DCS handbook. The heat load was assumed to be uniform across the full and partial length heater rods.

B.1.3.2 External DCS Structure Treatment

A “Standard K-ε Low-Re” flow model was applied to the air region within the DCS. Internal radiation was included in the air gas regions and the emissivity values were applied along the inner surfaces.

B.1.3.3 Input Parameters

The material properties for the solid parts in the model were taken from the DCS handbook. The effective properties for the heater rods were calculated based on volume weighted averaging of the Incoloy cladding and MgO. The Nichrome and carbon steel pins only represent a small percentage of the overall volume of the heater rod and were therefore neglected in the overall effective property calculation. The

effective material properties for the heater rods is listed in Table B.1. The properties for the helium and air gases are listed in Table B.2 and Table B.3, respectively.

Table B.1 Heater rod effective properties.

Temperature (K)	Density (kg/m^3)	Specific Heat (J/kg-K)	Thermal Conductivity (W/m-K)
300	3926.15	754.99	4.149
450	3926.15	878.32	4.922
650	3926.15	942.37	5.771
850	3926.15	978.80	6.605
1050	3926.15	1006.14	7.402

Table B.2 Helium properties.

Temperature (K)	Thermal Conductivity (W/m-K)	Viscosity (Pa-s)
100	0.0730	9.63E-06
120	0.0819	1.07E-05
140	0.0907	1.18E-05
160	0.0992	1.29E-05
180	0.1072	1.39E-05
200	0.1151	1.50E-05
220	0.1231	1.60E-05
240	0.1300	1.70E-05
260	0.1370	1.80E-05
280	0.1450	1.90E-05
300	0.1520	1.99E-05
350	0.1700	2.21E-05
400	0.1870	2.43E-05
450	0.2040	2.63E-05
500	0.2200	2.83E-05
600	0.2520	3.20E-05
650	0.2640	3.32E-05
700	0.2780	3.50E-05
750	0.2910	3.64E-05
800	0.3040	3.82E-05
900	0.3300	4.14E-05
1000	0.3540	4.46E-05

Table B.3 Air properties.

Temperature (K)	Thermal Conductivity (W/m-K)
294.26	0.0251
310.93	0.0264
422.04	0.0339
533.15	0.0405
644.26	0.0469
755.37	0.0532

B.1.3.4 Initial and Boundary Conditions

The heat load was assumed to be uniform across the full and partial length heater rods. External convection and radiation were applied along the vertical outer insulation and top horizontal surface of the shell assembly. The external convection coefficients were calculated based on natural convection coefficient correlations. Four test conditions are listed in Table B.4 and represent the four corners of the canister pressure and heat load cases. The ambient temperature was assumed to be at 300 K and the ambient pressure was assumed to be 83 kPa for all four cases. The flow straighteners were explicitly modeled for the detailed STARCCM+ model.

Table B.4 Four corner test conditions.

Case	Canister Pressure (kPa)	Heat Load (kW)
1	100	0.5
2	100	5
3	800	0.5
4	800	5

B.1.3.5 Symmetry

A full 360-degree mesh of the model was generated. This resulted in a very large mesh. For computational efficiency a quarter section model of the detailed geometry was also meshed. Symmetry boundaries were applied to the quarter model. Both the full 360 and quarter models were run for the 800 kPa canister pressure cases to compare and ensure that the quarter model was comparable to the full 360 model. Table B.5 compares the resulting mass flow of the air and PCT. Overall the quarter model behaves very similar to the full 360 model. For efficiency the quarter model was used exclusively. Figure B.1 shows the resulting mesh for the quarter model.

Table B.5 Mesh summary.

Case	Cell Count	Air Mass Flow	PCT
Full 360 Model @ 800 kPa and 0.5 kW	58481631	0.0206 kg/s	367
Quarter Model @ 800 kPa and 0.5 kW	12840684	0.0206 kg/s	367
Full 360 Model @ 800 kPa and 5 kW	58481631	0.0601 kg/s	654
Quarter Model @ 800 kPa and 5 kW	12840684	0.0601 kg/s	652

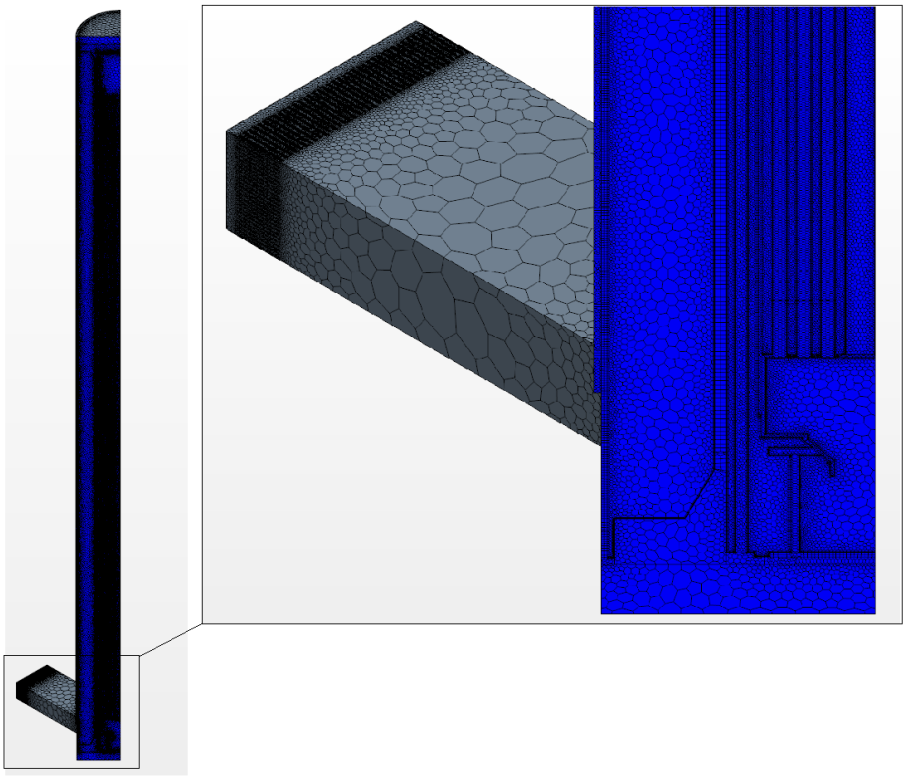

Figure B.1 Mesh for detailed quarter model – external view.

B.2 Model Description – Porous STARCCM+ Model

The detailed STAR-CCM+ model was simplified by replacing the flow straightener and fuel assembly regions with a porous region. This simplified the fuel assembly to a single region within the channel box. Removing the flow straighteners simplified the mesh near the flow inlets.

B.2.1 Representation of Fuel Assembly

The fuel assembly was represented with a porous media region. An effective thermal conductivity (k_{eff}) and porous flow loss coefficients were calculated for the fuel assembly region.

B.2.2 Representation of DCS Structures

The flow straightener was replaced with a porous region, and the porous flow loss coefficients were calculated.

B.2.3 Approximations and Treatments

B.2.3.1 Internal Fuel Assembly Treatment

A laminar model with the Boussinesq model was applied to the helium gas regions. The effective thermal conductivity of the homogeneous region representing the fuel assembly within the storage basket is derived using a model that assumes the heat transfer from the assembly is in the radial direction only, and consists only of conduction and thermal radiation. Convection heat transfer within the rod array is assumed negligible.

A 2-D model of the fuel assembly was set up in STAR-CCM+ to determine the radial effective fuel thermal conductivity. Two different STAR-CCM+ 2-D models were set up, one that included the full array of rods (full length and partial length rods) and one that did not include the partial length rods

(partial array). The measured emissivity of the zircaloy channel box was found to vary with axial position. For the 2-D models an average emissivity value was used. The emissivity was averaged over the length of the full array and partial array length for the respective STAR-CCM+ models. Figure B.2 and Figure B.3 show the resulting k_{eff} values for the full and partial array sections.

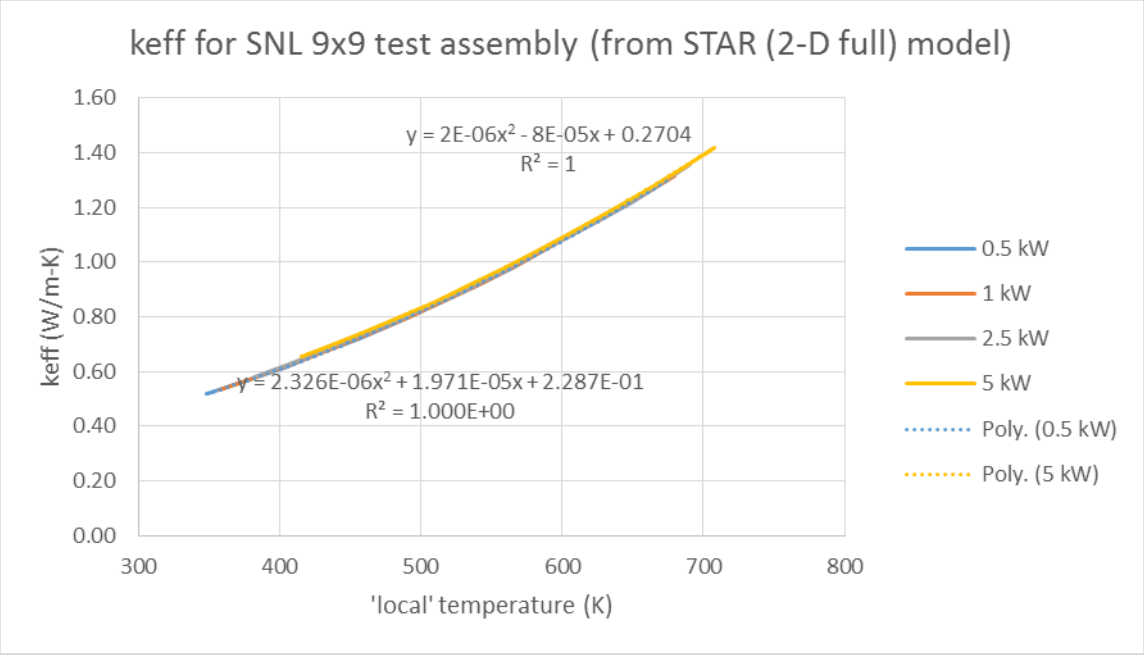

Figure B.2 Plot of local temperature versus k_{eff} for the full array.

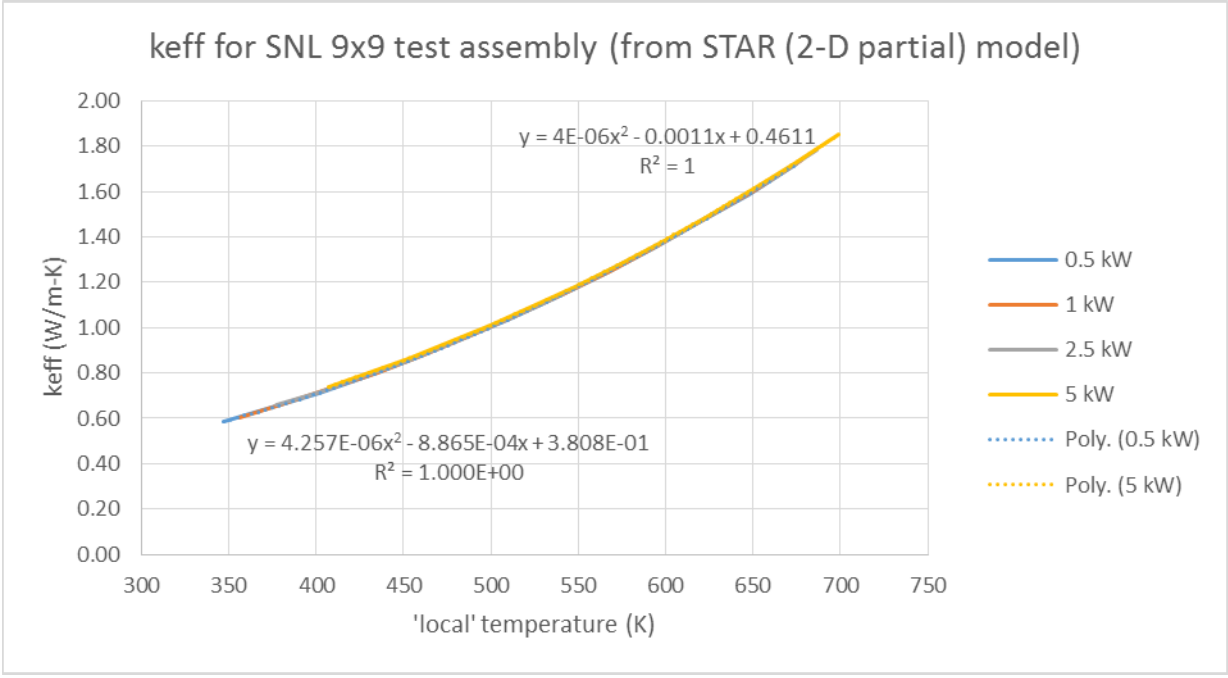

Figure B.3 Plot of local temperature versus k_{eff} for the partial array.

The axial k_{eff} value for the fuel region was calculated assuming a volume averaging scheme. The Incoloy, MgO, and helium volumes were considered when calculating effective axial thermal conductivity. Table B.6 lists the resulting axial k_{eff} for the fuel assembly.

Table B.6 Axial k_{eff} for fuel assembly.

Temperature (K)	Thermal Conductivity (W/m-K)
300	1.5590
450	1.8632
650	2.1989
850	2.5254
1050	2.8294

Submodels for the fluid region of the flow straightener and fuel assembly were constructed. These submodels were used to calculate the porous loss coefficients based on the pressure drop across each porous region. Table B.7 shows the resulting loss coefficients.

Table B.7 Calculated porous loss coefficients

Component	Axial Inertial Coefficient α (kg/m^4)	Axial Viscous Coefficient β (kg/m^3-s)
Fuel Assembly	21.869	22.191
Flow Straightener	7.666	48.795

B.2.3.2 External DCS Structure Treatment

The same conditions applied to the detailed STARCCM+ model were applied to the porous STARCCM+ model.

B.2.3.3 Input Parameters

The same material properties applied to the detailed STARCCM+ model were applied to the porous STARCCM+ model, with the exception of the porous region properties described in the previous sections.

B.2.3.4 Initial and Boundary Conditions

The same boundary conditions applied to the detailed STARCCM+ model were applied to the porous STARCCM+ model. The flow straightener was represented as a porous region with the loss coefficients described in the previous sections.

B.2.3.5 Symmetry

The porous media model was modeled as a quarter symmetry model, like the detailed STARCCM+ model.

B.2.3.6 Model Verification

A mesh sensitivity study was run with the porous media model to verify the mesh was sufficiently resolved. The initial mesh was refined such that the cell count was doubled across the air annulus. The refined case was also further refined to increase the cell count across the air annulus. Figure B.4 through Figure B.6 show a radial cross-section of the three different meshes.

Table B.8 gives the cell, face, and vertices count for the three meshes. All three meshes were run for the 800 kPa and 5 kW case. The resulting PCT and airflow for the three mesh cases are shown in Table B.9. The results show that the refined and very refined mesh produced similar results with a PCT of 684 K for each case. The default/coarse mesh also showed good agreement with the refined and very refined meshes with a resulting PCT within 1 degree of the other meshes. Airflow was slightly under predicted for the default/coarse mesh when compared with the refined and very refined cases.

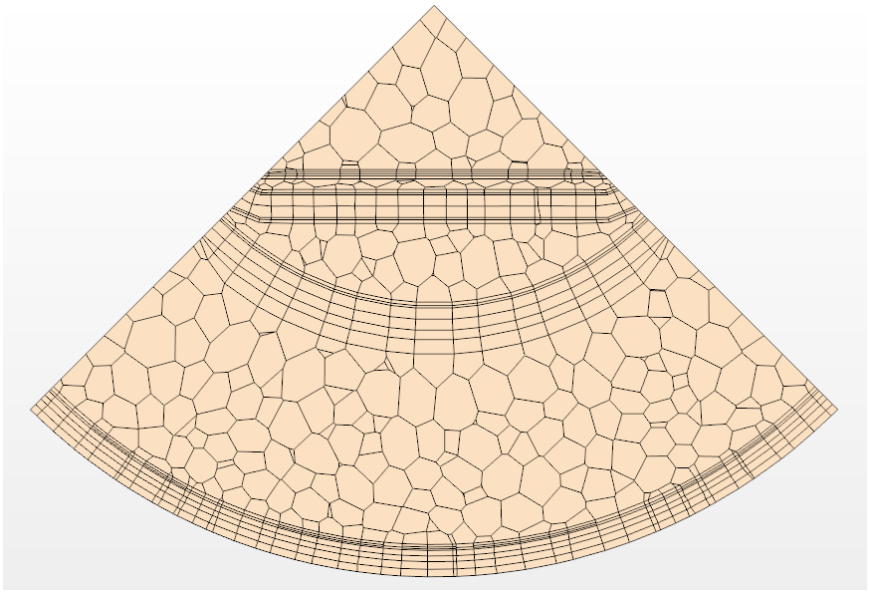

Figure B.4 Initial mesh configuration – radial cross-sectional view of DCS assembly.

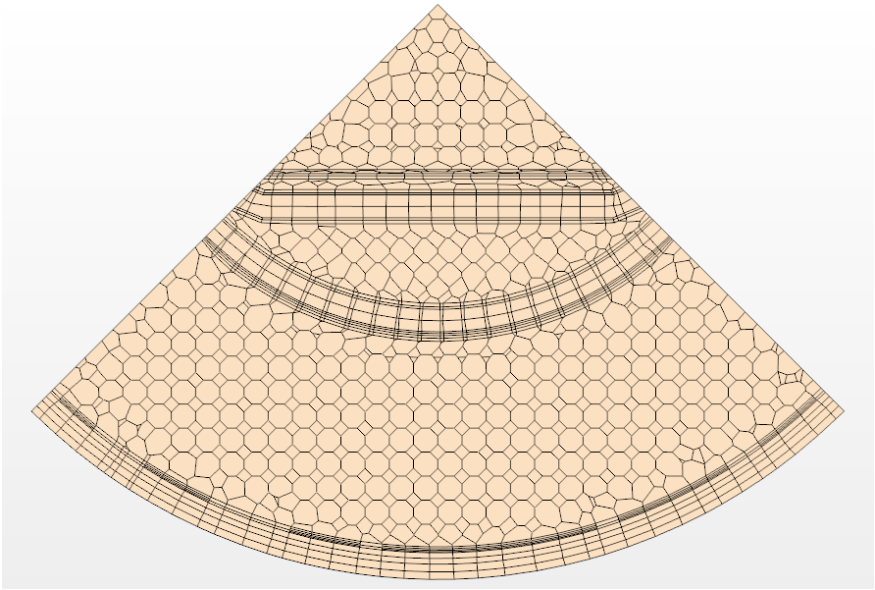

Figure B.5 Refined mesh configuration – radial cross-sectional view of DCS assembly.

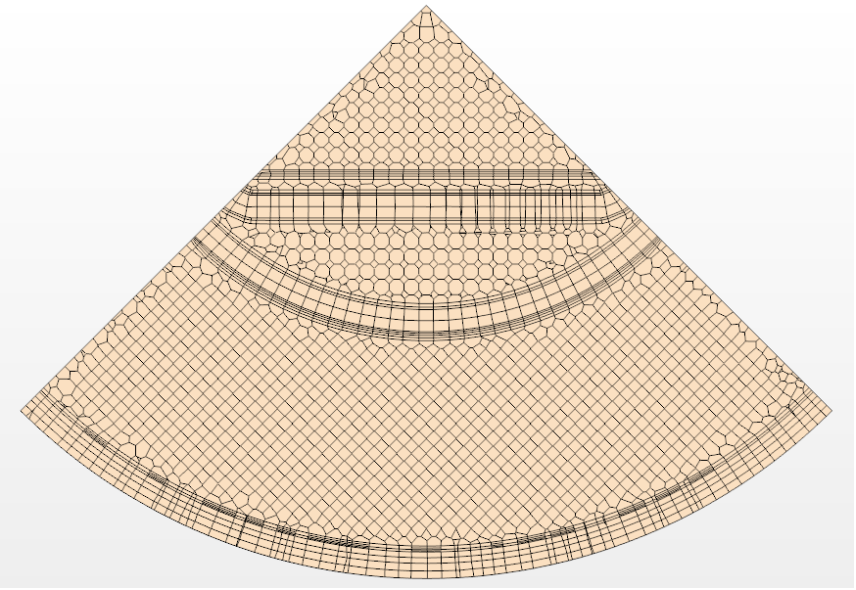

Figure B.6 Very refined mesh configuration – radial cross-sectional view of DCS assembly.

Table B.8 Mesh details for mesh sensitivity study.

Mesh	# Cells	# Faces	# Vertices
Default	308697	1370752	1090114
Refined	700002	3615718	2926131
Very Refined	2164639	12214134	10070256

Table B.9 Mesh sensitivity results at 800 kPa and 5 kW.

Mesh	PCT (K)	Air Mass Flow Rate (kg/s)
Default	683	0.0536
Refined	684	0.0595
Very Refined	684	0.0594

Using these results, an estimate of discretization error can be obtained by determining the Grid Convergence Index (GCI). The estimates of GCI shown in Table B.10. Note that the GCI is not a bounding error estimate, rather an indication of the relative error. For these two cases, it is prudent to use the larger of the two estimates. So, for a PCT on the order of 684 K, an estimate of the relative numerical error for the fine grid solution is 0.000837 × 683, which is 0.6 K.

Table B.10 Grid convergence index.

f_2	r	ε	E_1	GCI (fine grid)
Coarse mesh	1.91	0.000644	0.000242	0.000725
Medium mesh	1.46	0.000313	0.000279	0.000837

B.3 Model Description – COBRA-SFS Model

A summary of the COBRA-SFS model is in the outline form below. Please see our full report [Suffield *et al.*, 2019] for more detail.

COBRA-SFS has a structure and solution method that takes advantage of the features of a spent fuel storage system to provide high levels of detail in the fuel region and other important features and a coarse representation of the outer regions of the cask. The code uses what is often termed a 2.5-dimensional representation of the main region of the cask. This involves dividing the cask structures into several axial levels that are represented two dimensionally. In a typical system, a sufficiently detailed model will result in approximately 1000 user defined solid nodes. Adding additional refinement has not generally been shown to be useful and becomes impractical due to the large amount of connection definitions needed.

In the case of the DCS, the small size would make it possible to refine with an extreme amount of detail and stay within practical limits for the user and the code. However, for the purposes of this modeling exercise the simulator model was represented with a similar resolution of what might be used for a full cask, resulting in only 40 solid nodes. The node map for the simulator is shown in Figure B.7. With this approach, some conclusions can be drawn that are applicable to modeling full-scale systems.

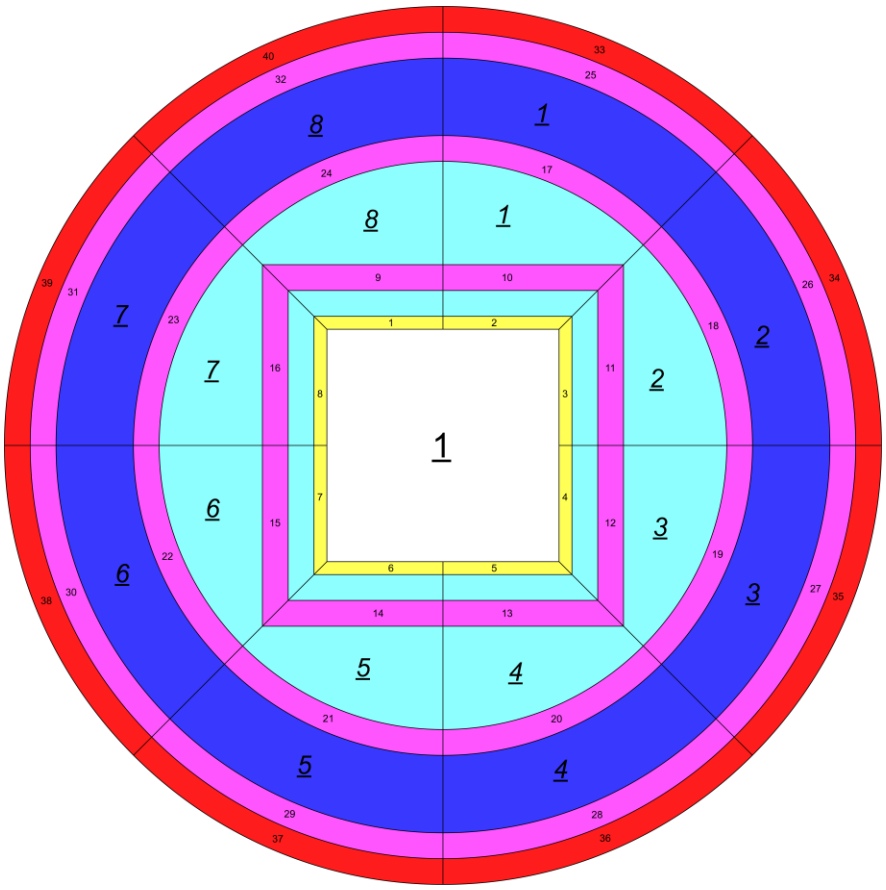

Figure B.7 Cross-section of the COBRA-SFS model representation of the DCS (not to scale).

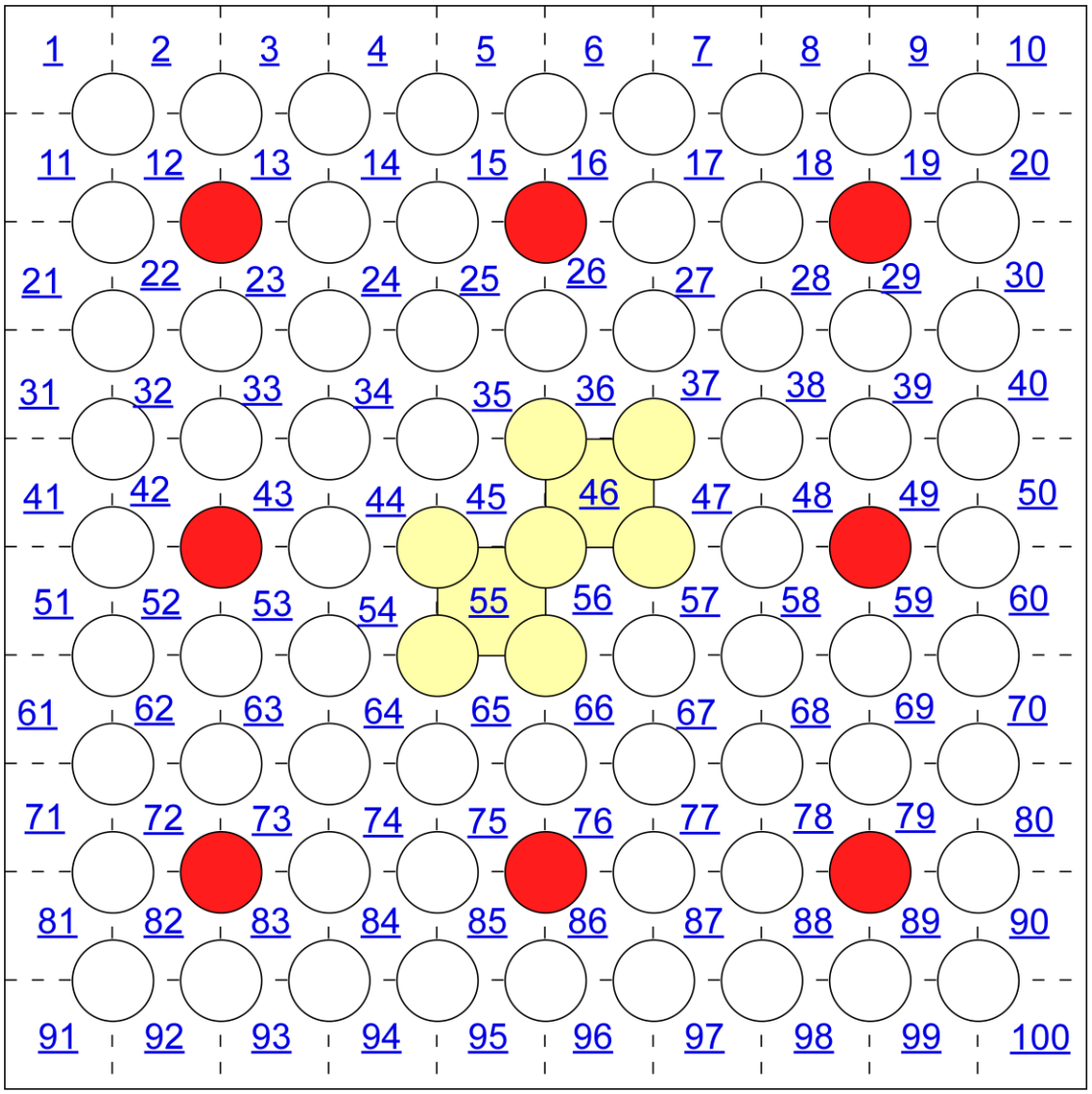

Figure B.8 Rod and subchannel array diagram for COBRA-SFS model of the 9×9 BWR fuel assembly (not to scale). Yellow represents water rods, red represents partial-length rods.

B.3.1 Representation of Fuel Assembly

Figure B.8 shows a representation of the 9×9 BWR fuel assembly used in the DCS. The highlighted rods and subchannels are the areas that the water rods occupy. For the COBRA-SFS model, these are modeled by blocking the channels where the water rods would be and turning off heat generation in the affected rods. This approach sufficiently represents both the true hydraulic resistance of the assembly and the heat generation distribution. There are also eight part-length rods in positions 11, 14, 17, 38, 44, 65, 68, and 71. Hydraulically, these rods are represented as full-length rods. This is appropriate for typical velocities in a spent fuel system and has minimum effects on the overall flow characteristics. The total heat generation in these rods is represented accurately. This results in a fully detailed radial heat generation rate, but due to the nature of the model the part-length rods will be represented with heat generation at a higher heat generation than is necessary.

B.3.2 Representation of DCS Structures

BWR assemblies are typically placed in dry storage with the fuel channel intact. This is also the case with the DCS. For COBRA-SFS modeling this presents two options for modeling the fluid region in between the fuel channel and basket. The standard practice would be to model the region as static helium along with a radiation connection. This approach neglects convection in this region and results in a conservative simplification for licensing analysis.

Alternatively, the model can be set up to solve for the fluid flow and resulting convection heat transfer along with the fluid conduction and surface to surface radiation. In a full-scale model this approach is usually considered to be too time intensive and not necessary for accuracy. In the case of the DCS model both approaches were tested, and results are presented for comparison.

B.3.3 Approximations and Treatments

B.3.3.1 Internal Fuel Assembly Treatment

Flow within the assembly is modeled as laminar or turbulent based on the Reynolds number of the channels. However, in practice this flow is primarily laminar. All heat transfer pathways are based off the given geometry. Radiation heat transfer is modeled with 2-D view factors that are then resolved axially. This approach will hold as long as the enclosures are relatively slender compared to their width. All flow losses are either derived from past modeling experience or accepted book values.

B.3.3.2 External DCS Structure Treatment

Unlike the other models, closure models are not applicable to COBRA-SFS.

B.3.3.3 Input Parameters

Solid material properties were taken directly from the materials and dimensions handbook provided by Sandia. The fluid properties were taken from a National Institute of Standards and Technology (NIST) reference as isobaric helium properties and air properties [NIST, 2019].

The fuel channel has a wide range of axial variation in emissivity with a minimum of 0.172 and a maximum of 0.655. This variation is atypical of BWR channels that have been in operation and are being placed in dry storage. In that case we would expect the profile to be much flatter and the magnitude to be close to the fuel's profile. This parameter becomes important at high temperatures because there is a strong radiation heat transfer path between the rods and the fuel channel. For best estimate modeling the average emissivity of 0.405 was used in the COBRA-SFS model. COBRA-SFS does not have a ready ability to vary the emissivity axially for this parameter, meaning there is no way to fully capture the effects of this simplification.

B.3.3.4 Initial and Boundary Conditions

The honeycomb device was treated with a loss coefficient. The external boundary condition uses a standard cylindrical convection correlation with no external heating due to radiation. The temperature boundaries match the average for each test case as reported in the Sandia test report [Durbin and Lindgren, 2017]. The pressure boundary is set to atmospheric pressure in Albuquerque, New Mexico, or 83 kPa.

B.3.3.5 Symmetry

COBRA-SFS modeling is done only with full symmetry models as standard practice.

B.4 Lessons Learned

Overall the measured PCT is in good agreement with this STAR-CCM+ detailed model. However, there are deviations in the high pressure and high heat load case (800 kPa and 5 kW). Comparing the elevations

at which the PCT occurred shows that the STAR-CCM+ detailed model elevations occur at similar locations to the measured data.

The STAR-CCM+ porous model predicted higher PCT values than the measured data for all four pressure heat load combinations, indicating that k_{eff} fuel assembly approach provides conservative PCTs. Using a split k_{eff} approach for the BWR fuel assembly was also shown to produce the best PCT agreement with the measured data for the porous model. The split k_{eff} approach calculated two different k_{eff} correlations for the full and partial array sections. Comparing the elevations at which the PCT occurred shows that the STAR-CCM+ porous model elevations also occur at similar locations to the measured data. The meshing study with the STAR-CCM+ porous media model showed that even the coarsest mesh provided reasonable PCT temperatures. This indicates that a larger model with a full cask/fuel assembly (instead of the single fuel assembly represented in the DCS) could be constructed at a computationally efficient element size with the porous media model.

The measured PCT is also in good agreement with the COBRA-SFS model, except for the high pressure and high heat load case (800 kPa and 5 kW). The COBRA-SFS cladding temperature profile is flat in comparison with STAR-CCM+ models. The COBRA-SFS model with the flatter profile varied significantly from the measured data for the low-pressure cases (100 kPa). This is most likely due to differences in how the partial length rods are handled in COBRA-SFS and an average emissivity value being applied axially over the channel box for the COBRA-SFS model. This model had a higher predicted air mass flow rate for the low heat load cases (0.5 kW) and a slightly lower air mass flow rate for the high heat load cases (5 kW).

B.5 References

Durbin, S.G. and E.R. Lindgren, “Thermal-Hydraulic Results for the Boiling Water Reactor Dry Cask Simulator,” SAND2017-10551R, Sandia National Laboratories, Albuquerque, New Mexico, September 2017

National Institute of Standards and Technology, https://www.nist.gov.

Suffield, S.R., D.J. Richmond, and J.A. Fort. “Modeling of the Boiling Water Reactor Dry Cask Simulator,” PNNL-28424, Pacific Northwest National Laboratory, Richland, Washington, January 2019.

APPENDIX C – CIEMAT MODEL INFORMATION

The thermal-fluid dynamic analysis of the cask storage system mock-up has been carried out with the CFD FLUENT 18.0 code. The FLUENT 18.0 solver provides numerical solutions for the Navier-Stokes equations. To solve these equations, a RANS (Reynolds Averaged Navier-Stokes) method of two equations (Reynolds stress equations) was used for the air flow. This method adds two unknowns – the turbulent kinetic energy and either the turbulence dissipation rate or the specific dissipation.

C.1 Model Description

C.1.1 Representation of Fuel Assembly

The fuel assembly has been approximated as a porous rectangular parallelepiped with internal heat generation. The approach requires characterizing the porous media by means of an effective thermal conductivity and a pressure drop. In order to derive a fuel assembly effective thermal conductivity, a detailed 2D model was developed according to best practice guidelines issued by the NEA [Mahaffy *et al.*, 2015]. To perform the hydraulic analogy, the viscous and inertial resistance parameters found in [Holtec International, 2014] have been used in the Darcy-Brinkman equation.

C.1.2 Representation of DCS Structures

The grid has been built up according to the flow characteristics and the turbulence modeling adopted. In total, the fluid domain has been defined by 850 thousand polyhedral and hexahedral cells. The mesh meets quality standards based on maximum aspect ratio (25), minimum orthogonal quality (0.2) and maximum skewness (0.77). The only structure defined external to the fuel assembly is the honeycomb flow straightening element, which is modeled as a porous media.

C.1.3 Approximations and Treatments

C.1.3.1 Internal Fuel Assembly Treatment

Based on the preliminary analysis, the laminar model has been selected to simulate the helium flow. The effective thermal conductivity includes conduction and radiation – thus, inside the fuel assembly, the radiation heat transfer is deactivated. The viscous and inertial resistance parameters have been found in [Holtec International, 2004].

C.1.3.2 External Fuel Assembly Treatment

The k-ω SST turbulence model has been selected to simulate the air flow. This turbulence model has been used despite the Reynolds number being close to the low bound of the turbulent regime because of its capability to describe the flow behavior in the viscous sub-layer of the boundary layer without needing any extra damping function.

C.1.3.3 Input Parameters

Helium thermo-physical properties have been tabulated as a function of temperature, except for helium density, which is approximated as an ideal gas (i.e., T and P dependent). The channel box emissivity has been expressed as a function of height (Figure C.1), as suggested in the benchmark.

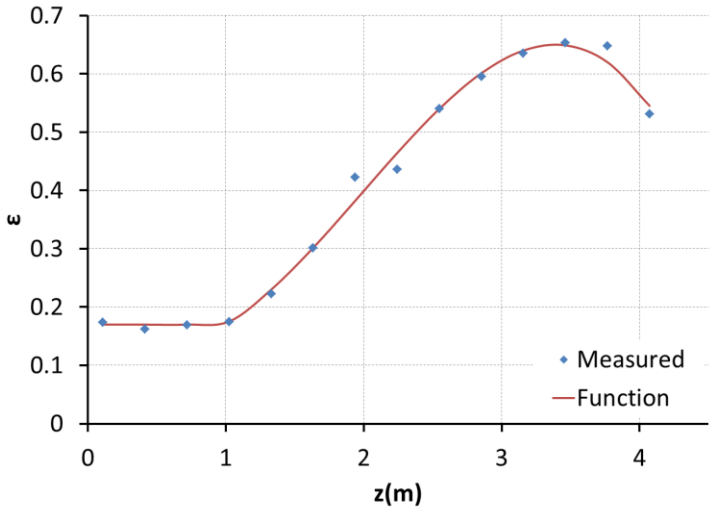

Figure C.1 Channel box emissivity as a function of height.

C.1.3.4 Initial and Boundary Conditions

The convective heat transfer coefficients at the outer surfaces have been calculated with the Churchill and Chu correlations of natural convective heat transfer. The bottom blind flange has been considered adiabatic. The honeycomb flow straightening element was modeled as a porous media – the viscous and inertial resistances are detailed in Table C.1.

Table C.1 Viscous and inertial resistances of the honeycomb flow straightening element.

	Direction X	Direction Y	Direction Z
Viscous Resistance	1.53E+05	2.00E+06	2.00E+06
Inertial Resistance	0	0	0
Porosity			0.81

For the thermal boundary conditions, the heat transfer coefficient is defined by the following equations:

$$HTC = 0 \text{ for } T_w < 301$$

$$HTC = 4.3501E\text{-}6 \cdot T_w^3 - 4.8593E\text{-}3 \cdot T_w^2 + 1.8281 \cdot T_w - 2.2661E\text{-}2 \text{ for } T_w > 301$$

The free stream temperature is 300 K, and the internal emissivity, wall thickness, and heat generation rate are all set to 0.

For the radiation boundary conditions, the boundary condition type is set to opaque, and the diffuse fraction value is set to 1.

For the pressure inlet, the following initial and boundary conditions are used. For the momentum, the reference frame is set to absolute, the gauge total pressure and the supersonic/initial gauge pressure are set to 0. The direction specification method is set normal to the boundary. The turbulence specification method is based on the turbulent intensity and hydraulic diameter, which are set to 5.2% and 0.141 m, respectively. For the thermal boundary condition, the total temperature is set to 300 K, and for the radiation boundary condition, the boundary temperature is set based on the external black body temperature method, with an internal emissivity of 1.

For the pressure outlet, the following initial and boundary conditions are used. For the momentum, the reference frame, gauge total pressure, and supersonic/initial gauge pressure are set to the same values as the pressure inlet case. The backflow direction specification method is set normal to the boundary, while the turbulent intensity for the backflow is set to 5% and the backflow hydraulic diameter is set to 0.145 m. For the thermal boundary condition, the backflow total temperature is set to 300 K, and for the radiation boundary condition, the boundary temperature is set based on the external black body temperature method, with an internal emissivity of 1.

C.1.3.5 Symmetry

The computational domain has been restricted to $1/8^{th}$ of the whole circular cross section of the DCS.

C.2 Lessons Learned

The comparisons of experiment versus model axial temperature profiles show that the predicted temperature profiles agreed reasonably with measurements. The maximum deviations were noted to happen for the maximum temperature at the lower portion of the system (0.5 m) under high power. In relative terms, these deviations are more pronounced at high pressure, as the deviation becomes nearly 20% of the total temperature rise (300 K → 550 K, roughly). For the low power case, the situation changes – the largest relative deviations occurred in minimum temperatures at high pressures (about 10%) at the upper part of the system.

In addition to the best estimates, a sensitivity case was carried out to check the effect of using other turbulence models for the air flow. The Nagano Low Reynolds turbulence model was activated – no major differences were observed when switching turbulence modeling. This being said, other sensitivity analyses conducted using the k-ε RANS model resulted in noticeable deviations, so not just any RANS should be used for the system under analysis. Either k-ω SST or the Low Reynolds k-ε model are recommended.

Some other sensitivity analyses were performed. The main outcome from them is that the pressure drop through the system is an important variable to catch when using the porous medium approximation, whereas the effective thermal conductivity has substantially less significance.

The model used (porous medium) is highly sensitive to the turbulence model used in the air channel, so the use of the k-w SST turbulence model is recommended (although the k-ε Low Reynolds also gives good results). Estimation of the pressure loss along the porous medium is critical to obtaining accurate results.

Even though the PCT can be said to be reasonably estimated in all cases, under high thermal loads predicted temperatures show major discrepancies with respect to measurements (steep data gradients vs. rather uniform temperature predicted profiles). Such a difference vanishes when low thermal loads are modeled. This effect should be explored further – a potential facility effect cannot be discarded. The modeling leads to an overestimate of heat removal to the UHS, so that under high thermal load thermal profiles are somewhat underestimated (except when the data shows an asymptotic trend).

C.3 References

Holtec International, “Pressure loss characteristics for in-cell flow of helium in PWR and BWR MPC storage cells,” HI-2043285, Holtec International, Marlton, NJ, 2004.

Mahaffy, J., B. Chung, F. Dubois, F. Ducros, E. Graffard, M. Heitsch, M. Henriksson, E. Komen, F. Moretti, T. Morii, P. Mühlbauer, U. Rohde, M. Scheuerer, B.L. Smith, C. Song, T. Watanabe, and G. Zigh, “Best practice guidelines for the use of CFD in Nuclear Reactor Safety Applications – Revision,” NEA/CSNI/R(2014)11, Nuclear Energy Agency Committee on the Safety of Nuclear Installations, February 2015.

This page is intentionally left blank.

APPENDIX D – ENUSA-UPM MODEL INFORMATION

The purpose of this appendix is to introduce the model construction, structure, approximations and hypotheses used to create the aboveground Dry Cask Simulator (DCS) simulation model by ENUSA Industrias Avanzadas S.A., S.M.E in collaboration with Universidad Politécnica de Madrid (UPM). To this end, the first part of this appendix includes a brief description of the Computational Fluid Dynamic (CFD) code used in the simulations, followed by the model description and conclusions.

Four cases have been simulated with the following conditions: 0.5 kW at 100 kPa, 5 kW at 100 kPa, 0.5 kW at 800 kPa, and 5 kW at 800 kPa.

D.1 Introduction to Code

CFD codes have been developed over the last years to become a reliable tool for analyzing complex flow situations. Therefore, a commercial CFD code, STAR-CCM+ version 13.02.011 has been used to simulate the DCS test.

CFD codes use finite volume numerical methods that solve an integral form of the fluid governing equations for mass, momentum and energy, using body-fitted meshes. A brief description of the main characteristics of a CFD are summarized in Table D.1. For more information about the STAR-CCM+ CFD code, see [SIEMENS, 2018].

Table D.1 CFD characteristics.

Numerical Method	Finite volume
Turbulence	Modeled (in conservation equations of energy and momentum)
Heat transfer	Calculated
Friction	Calculated
Computational cost	High dependence from model to model

D.2 Model Description

The DCS is divided into two main regions: the vessel and the air entrance. The cylindrical pressure vessel filled with helium represents the canister. Inside of the vessel, a single 9×9 BWR fuel assembly is deployed inside of a representative storage basket. External to the canister, air flow is buoyantly induced in the annulus between the canister and outer shell. The four air inlets at the bottom part of the DCS have honeycomb elements inserted to straighten the flow. For more details, see the explanation in the main body of this document.

The model chosen to simulate the DCS in STAR-CCM+ consists of an explicit model where all fuel rods and water rods have been modeled. The test assembly has been modeled starting at the inner cladding and extending to the outer shell – see Figure D.1 and Figure D.2. To reduce modeling efforts, symmetry, hypotheses and approximations have been applied to the model.

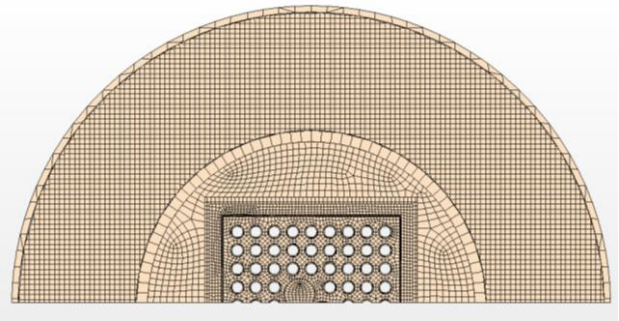

Figure D.1 STAR-CCM+ explicit model fuel assembly and DCS structure axial cross-section.

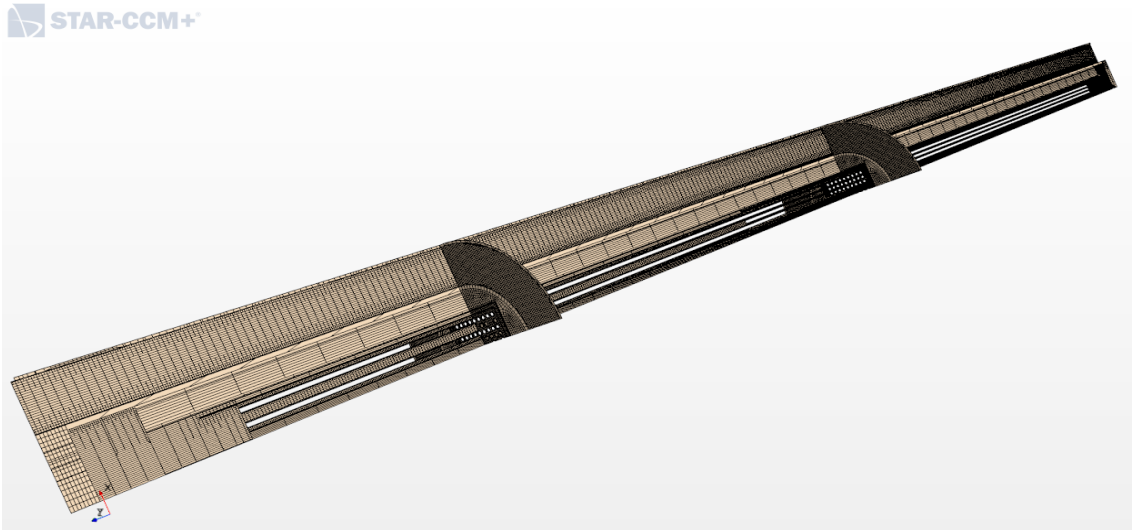

Figure D.2 STAR-CCM+ explicit model, ¼ symmetry mesh.

D.2.1 Representation of Fuel Assembly

The 9×9 BWR fuel assembly has 74 heater rods (66 of them full length rods and 8 partial length rods), and 2 water rods. As can be seen in Figure D.1 and Figure D.2, the mesh of the simulation model extends from the cladding of each rod (full and partial length rods) to the outer shell. Heat flux is applied at the inner face of the cladding. Water rods have also been modeled, allowing the movement of helium inside.

One of the main advantages of using an explicit model is the ability to obtain the cladding temperature on a rod-by-rod basis in the simulation. Cladding temperature is a key parameter to prevent unacceptable cladding degradation during storage, such as creep and hydride reorientation that can appear at high cladding temperatures. This detailed approach also allows the use of fewer assumptions, such as fixing a thermal conductivity or a pressure drop in the fuel area. As for a disadvantage, creating an explicit model requires more work regarding meshing and geometry modeling for the user.

D.2.2 Representation of DCS Structures

Materials and dimensional data have been taken from the Handbook provided by Sandia National Laboratories [Lindgren and Durbin, 2017]. A detailed structure of the model in STAR-CCM+ is represented in Figure D.3.

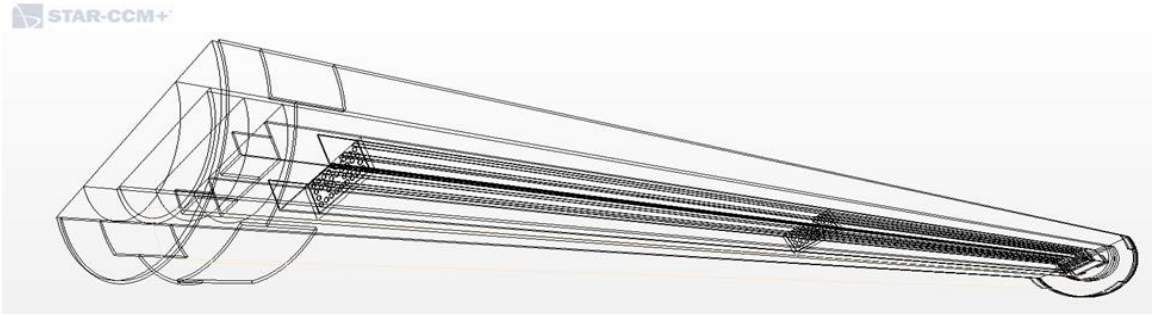

Figure D.3 Explicit DCS modeling structure, ½ symmetry.

The flow regime inside the DCS has been estimated to be turbulent and therefore it has been modeled as a RANS turbulent model – the Realizable K-ε (Shear Driven), which was chosen by taking into account sensitivity studies done by ENUSA Industrias Avanzadas S.A., S.M.E and UPM for other containers [Benavides *et al.*, 2018].

The physical and numerical models used in the simulation are summarized in Table D.2.

Table D.2 STAR-CCM+ physical and numerical scheme.

Discretization	2nd order
Time discretization	Steady State
Gas model	Ideal gas (helium, air)
Solid material properties	Defined in the DCS handbook
Thermal properties	Dependent on temperature for both fluids and solids (viscosity, thermal conductivity…)
Turbulence model	Realizable k-ε (Shear Driven)
Wall function	Two-layer all y+ wall treatment
Radiation model	S2S
Reference pressure	83.3 kPa (Ambient pressure in Albuquerque, NM)
Mesh	Directed Mesh + Automated Mesh (2.600.000 cells)

D.2.3 Approximations and Treatments

To reduce computational cost and modeling efforts, some approximations and additional hypotheses have been taken into account in the DCS model simulation. They are summarized in the following sub-sections.

D.2.3.1 Internal Fuel Assembly Treatment

Fuel rods have been modeled starting at the inner cladding and extending to the outer shell. The fuel rods and water rods are modeled as hollow cylinders (Figure D.4) with heat flux applied at the inner face of the cladding. The spacers were not simulated due to the additional computational cost and the flow regime inside the DCS has been treated as turbulent for both air and helium.

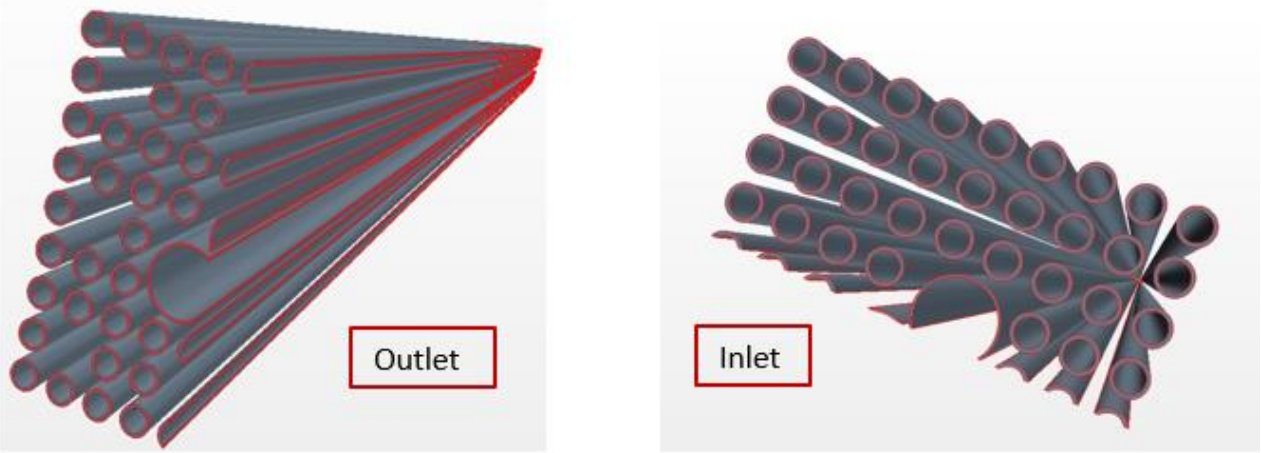

Figure D.4 Model partial and full-length rods, ½ symmetry.

D.2.3.2 External DCS Structure Treatment

The treatment of the external DCS structures is summarized in Table D.2. The air flow was accounted for by a shear-driven realizable k-ε turbulence model, with a two-layer all y+ wall treatment.

D.2.3.3 Input Parameters

Material property input parameters such as temperature, density, thermal conductivity, hemispherical total emissivity (HTE) and specific heat capacity for the solid cask material have been taken from the DCS Handbook [Lindgren and Durbin, 2017]. Air and helium thermal properties used in the simulation are summarized in [Bergman *et al.*, 2011]. The properties of both fluids have high dependence on temperature, and that is the reason why they have been modeled as ideal gases.

The experiments were conducted in Albuquerque, New Mexico, where the local ambient atmospheric pressure is 83.3 kPa – this is used as the reference pressure in the simulation. The ambient temperature is 298.15 K.

D.2.3.4 Initial and Boundary Conditions

The inlet honeycomb elements have been modeled as a pressure jump between air inlets/outlets (stagnation inlet) calculated on the basis of data provided by Sandia National Laboratories.

The outside vessel Heat Transfer Coefficient (HTC) has been obtained from correlations and takes into account the radiation to the environment. The top and bottom of the canister have been considered adiabatic (as isolated walls), as suggested in the test specifications.

D.2.3.5 Symmetry

As the model is symmetric, half of the geometry has been modeled to reduce meshing and modeling efforts. Invoking symmetry leads to a decreased number of cells in the mesh and directly reduced computational cost.

In Figure D.1 and Figure D.2, the geometry and mesh used in the simulations are represented.

D.2.3.6 Model Verification

Regarding model verification, no sensitivity analysis nor grid independence convergence have been done due to the short time available to create the models. Introducing a grid convergence study and sensitivity analysis would let us know the discretization error.

D.3 Lessons Learned

This section provides a general overview and discussion of results obtained, which focused on air mass flow rate and peak cladding temperature (PCT), and includes lessons learned and areas of improvement.

Regarding air mass flow rate results, the minimum differences between test measurements and simulation results are for the low power (0.5 kW) and high pressure (800 kPa) case with a relative error of 3.5%.

In a previous simulation, the error obtained for the low power (0.5 kW) and high pressure (800 kPa) case gave an error of 80%, so reviewing and improving this simulation was one of the first goals. After checking different parameters including boundary conditions and meshing, the air pressure differential between the pressure inlet and pressure outlet (both initially set to 0 Pa absolute) was found to be incorrect. Although the code calculates hydrostatic pressure in the computational domain, the boundaries do not compensate for the hydrostatic pressure. This results in certain downward flow from the outlet to the inlet (if the vessel had not been heated the flow would flow from outlet to inlet). This can be fixed by initializing the pressure inlet with a pressure of 4.4 Pa (approximately the hydrostatic pressure) – with this, the 800 kPa and 5 kW case went from an error of 80% in mass flow to a more reasonable value of 3.5%.

For the low power (0.5 kW) and low pressure (100 kPa) case the relative error is approximately 25% in air mass flow rate. It should be noted that this result corresponds to the value obtained before the correction of the pressure inlet explained in the previous paragraph had been taken into account. The results are expected to improve by introducing this pressure in the simulation.

PCT results showed good agreement with experimental measurements yielding a maximum relative error of 3% for the high power (5 kW), low pressure (100 kPa) case. Due to setting an air pressure jump, the PCT results are relatively unaffected compared to the effect on air mass flow rate. When setting a pressure at the inlet, the relative error in PCT improved from 2.6% to 0.3% for the 800 kPa and 0.5 kW case.

Model temperature comparisons to the experimental results showed a slight deviation in the modeling results at the top of the fuel axial level, which is directly related to the top of the canister being considered adiabatic due to an isolated wall (as stated in the DCS Handbook [Lindgren and Durbin, 2017]). This approach has proven to significantly underestimate heat transfer near the top of the assembly. All four cases use this approach, with the 0.5 kW and 100 kPa showing the largest discrepancy in the temperatures at the top axial level.

There is a big discrepancy between the experimental results and the simulation model's calculation of the maximum fuel temperature as a function of axial level for the 5 kW and 800 kPa case. One hypothesis to explain this discrepancy is that treating the helium as an ideal gas at high pressures might not be correct and leads to the significant error shown above. The absence of the spacers in the assembly might offer another explanation for the differences found between the model and the experimental data. Future work is needed to test this hypothesis.

Despite the particular cases described previously, the simulation results have good agreement with the test measurements, particularly for peak cladding temperature, where the maximum relative error is 3%.

As main areas for improvement, sensitivity studies for turbulence models that have been done for other works (see [Benavides *et al.*,2018]), addressing compressibility issues for the helium gas model at high pressures, and introducing the spacers in the assembly model are some areas of interest for further exploration.

The main lesson learned during the modeling of the DCS is that it is possible to predict both PCT and overall temperature distribution using CFD calculations. Nonetheless, there is still work to be done – the sensibility of the mass flow to small changes in the inlet pressure show that a degree of testing is required when testing natural convection flows. Future work needs to be done regarding the higher-pressure

helium cases where temperature distribution is under-predicted in the simulations (although the PCT is fairly accurate).

D.4 References

Benavides, J., G. Jimenez, M. Galbán, and M. Lloret, "STAR-CCM+ Simulation of a Spent Fuel Dry Cask External Cooling By Natural Convection," TopFuel Prague, Sept. 2018.

Bergman, T.L., A.S. Levine, F.P. Incropera, and D.P. Dewitt, "Fundamentals of Heat and Mass Transfer," 7th ed. Wiley, Hoboken, NJ, 2011.

Lindgren, E.R. and S.G. Durbin, "Materials and Dimensional Reference Handbook for the Boiling Water Reactor Dry Cask Simulator," SAND2017-13058 R, Sandia National Laboratories, Albuquerque, New Mexico, November 2017.

STAR-CCM+ 13.02 User Guide, SIEMENS, 2018.